AMERICAN METEOROLOGICAL SOCIETY

Monthly Weather Review

EARLY ONLINE RELEASE

This is a preliminary PDF of the author-produced manuscript that has been peer-reviewed and accepted for publication. Since it is being posted so soon after acceptance, it has not yet been copyedited, formatted, or processed by AMS Publications. This preliminary version of the manuscript may be downloaded, distributed, and cited, but please be aware that there will be visual differences and possibly some content differences between this version and the final published version.

The DOI for this manuscript is doi: 10.1175/2008MWR2666.1

The final published version of this manuscript will replace the preliminary version at the above DOI once it is available.

Quantifying the Imprint of a Severe Hector Thunderstorm during ACTIVE/SCOUT-O3 onto the Water Content in the Upper Troposphere/Lower Stratosphere

CHARLES CHEMEL[⋆], MARIA R. RUSSO[+], JOHN A. PYLE[+], RANJEET S. SOKHI[⋆], AND CORNELIUS SCHILLER[#]

[⋆]*Centre for Atmospheric & Instrumentation Research, University of Hertfordshire, Hatfield, UK*

[+]*Centre for Atmospheric Science, University of Cambridge, Cambridge, UK*

[#]*Institute for Chemistry and Geodynamics (ICG-I), Forschungszentrum Jülich, Jülich, Germany*

Submitted, *Monthly Weather Review,* 23 May 2008

October 12, 2008

Corresponding author address:

Dr. Charles Chemel, Centre for Atmospheric & Instrumentation Research, University of Hertfordshire, College Lane Campus, Hatfield, Herts AL10 9AB, UK.

E-mail: c.chemel@herts.ac.uk

ABSTRACT

The development of a severe Hector thunderstorm that formed over the Tiwi Islands, north of Australia, during the ACTIVE (Aerosol and Chemical Transport in tropIcal Convection)/SCOUT-O3 (Stratospheric-Climate links with emphasis On the Upper Troposphere and Lower Stratosphere) field campaign in late 2005, is simulated by the ARW (Advanced Research core of the Weather Research and Forecasting (WRF) model) and UK Met Office UM (Unified Model) models. The general aim of this paper is to investigate the role of isolated deep convection over the Tropics in regulating the water content in the upper troposphere/lower stratosphere (UT/LS).

Using a horizontal resolution as fine as 1 km, the numerical simulations reproduce the timing, structure, and strength of Hector fairly well when compared with field campaign observations. The sensitivity of results from ARW to horizontal resolution is investigated by running the model in a large-eddy simulation mode with a horizontal resolution of 250 m. While refining the horizontal resolution to 250 m leads to a better representation of convection with respect to rainfall, the characteristics of the Hector thunderstorm are basically similar in space and time to those obtained in the 1-km horizontal resolution simulations.

Several overshooting updraughts penetrating the tropopause are produced in the simulations during the mature stage of Hector. The penetration of rising towering cumulus clouds into the LS maintains the entrainment of air at the interface between the UT and the LS. Vertical exchanges resulting from this entrainment process have a significant impact on the redistribution of atmospheric constituents within the UT/LS region at the scale of the islands. In particular, a large amount of water is injected in the LS. The fate of the ice particles as Hector develops drives the water vapor mixing ratio to saturation by sublimation of the injected ice particles, moistening the air in the LS. The moistening was found fairly significant above 380 K and averaged about 0.06 ppmv in the range 380–420 K for ARW. As for UM, the moistening was found much larger (about 2.24 ppmv in the range 380–420 K) than for ARW. This result confirms that convective transport can play an important role in regulating the water vapor mixing ratio in the LS.

1. Introduction

The characteristics of the upper troposphere/lower stratosphere (UT/LS) region are intrinsically determined by those of both spheres. The balance of processes that regulate its dynamical, radiative and chemical characteristics is at the heart of the debate on UT/LS exchanges. In particular, the quantification of the respective role of convective overturning in the troposphere and radiative and/or diabatic overturning in the stratosphere in determining the entry of atmospheric constituents into the LS is still a polemical issue for air quality and climate applications (e.g. Forster and Shine 1999; Kirk-Davidoff et al. 1999). The troubling uncertainty regarding the balance of processes contributes to the uncertainty of trends in the future composition of the atmosphere.

Riehl and Malkus (1958) showed for the first time that towering cumulus clouds that reach the tropopause have a large impact on the energy balance of the tropical atmosphere. The height to which tropical convection reaches and affects the composition of the UT/LS region remains uncertain. The transition layer where both tropospheric and stratospheric processes interact is usually referred to as the tropical tropopause layer (TTL) (see for instance Atticks and Robinson 1983; Holton et al. 1995; Highwood and Hoskins 1998). This transition zone is typically defined as the region extending from the main convective outflow (10–14 km, Folkins 2002) up to the cold point tropopause (16–17 km, Highwood and Hoskins 1998). The cold point is usually defined as the level of the minimum temperature in the vertical temperature profile. Note that the position of the cold point thus defined is very close to the position of the minimum water vapor saturation mixing ratio (e.g. Dessler 1998; Zhou et al. 2001). The TTL region is key for most air entering the stratosphere. Deep convective clouds occasionally reach the height of the TTL and even the

deepest clouds often penetrate up to the cold point (e.g. Danielsen 1982, 1993). By destabilizing the TTL, convective updraughts affect the vertical transport of atmospheric constituents into the stratosphere. Indeed, several studies have clearly indicated a predominant role for such convective events in determining temperature (Sherwood et al. 2003; Kuang and Bretherton 2004; Robinson and Sherwood 2006), water vapor (Sherwood and Dessler 2000, 2001; Read et al. 2004), and other tracer profiles (Dessler 2002) near the cold point. Nonetheless, some studies have shown that most of tropical convection does not extend beyond 14 km in altitude (e.g. Folkins et al. 1999). This altitude is often referred to as the mixing barrier, above which the effects of convection drop off rapidly. The altitude of the mixing barrier roughly corresponds to the lower boundary of the TTL. Hence the cold point has been suggested as a stratospheric feature which is decoupled from convection (e.g. Thuburn and Craig 2002). In that case, cross-tropopause transport is a result of large-scale ascent (see for instance Reid and Gage 1996). This mechanism still implies air to cross the level of zero net radiative heating (denoted by LZH hereafter), above which air rises and below which air descends. Note that this picture does not require neither exclude overshooting convection as an important mechanism for cross-tropopause transport. A thorough discussion, further focused on water vapor entry in the stratosphere, is presented in § 5.

As stated above, deep convection over the Tropics is thought to play a significant role in determining UT/LS exchanges. Basically, there are three regions of intense deep convective activity over the Tropics, namely South America, Central Africa, and the Maritime Continent, which includes the Indonesian archipelago and northern Australia. Tropical convection is especially intense over the Maritime Continent during the buildup of the monsoon (e.g. Keenan et al. 1994). During the Australian pre-monsoon season (typically in November–December), severe storms are usually tied to the islands on the south-east extremity of the Maritime Continent, which

are strongly influenced by coastal and diurnal effects. Thunderstorms occur almost every afternoon over the islands during this period (Keenan et al. 1990). It is during the mature part of the buildup just prior to the monsoon onset when the storms reach their maximum intensity (May and Ballinger 2007). Note that during the monsoon season, convection peaks usually over the ocean in the early afternoon and over the land in the early morning (see for instance Keenan et al. 1989a; Chen and Houze, Jr. 1997). The difference in the timing of convection is mainly due to day to night variations in radiative heating between cloudy and clear-sky regions (Gray and Jacobson, Jr. 1977) and in radiative cooling of cloud tops (Kraus 1963), to the semidiurnal solar atmospheric tide (Brier and Simpson 1969) over the ocean, and to coastal and topographic effects over the land (Houze, Jr. et al. 1981). Also, monsoon convection usually produces more rain, with a larger contribution of stratiform rain, over a larger area, but there are fewer vigorous convective cells (May and Ballinger 2007).

There have been numerous insightful observational studies devoted to deep tropical convection over the western equatorial Pacific (namely in the range 100–180 °E). For instance, the AMEX (Australia Monsoon EXperiment, Holland et al. 1986), EMEX (Equatorial Mesoscale EXperiment, Webster and Houze Jr. 1991), and STEP (Stratosphere-Troposphere Exchange Project, Russell et al. 1993) programs were designed to investigate convective mesoscale systems in the monsoonal flow north of Australia. These three programs dealt mainly with mesoscale processes, and did not detail the isolated thunderstorms that develop over the islands during the pre-monsoon season. The ITEX (Island Thunderstorm EXperiment, Keenan et al. 1989b) and MCTEX (Maritime Continent Thunderstorm EXperiment, Keenan et al. 2000) were the first programs to examine in detail these storms. These programs focused on the giant thunderstorms (known as Hector thunderstorms) that develop over the Tiwi Islands, around 80 km north of Darwin, Australia.

Deep convection was found to be initiated mainly by cold air pool interactions and convergence of penetrating sea-breeze flows (e.g. Carbone et al. 2000). The DAWEX (Darwin Area Wave EXperiment, Hamilton et al. 2004) program also investigated deep convection in the area of Darwin, and was further dedicated to the study of tropical internal gravity waves and their relation to tropospheric convection. In late 2005 and early 2006, the Darwin area hosted two intensive observation periods (IOPs), which involved three consortium programs, namely SCOUT-O3 (Stratospheric-Climate links with emphasis On the Upper Troposphere and Lower Stratosphere, Vaughan et al. 2008), TWP-ICE (Tropical Warm Pool International Cloud Experiment, May et al. 2008), and ACTIVE (Aerosol and Chemical Transport in tropIcal ConVEction, Vaughan et al. 2008). SCOUT-O3 was held in November–December 2005 and was focused on deep convection and its relation to UT/LS exchanges and ozone chemistry. TWP-ICE was conducted in January–February 2006 and designed to relate cirrus properties to characteristics of both the environment and deep convection. As for ACTIVE, it was held concurrently with both SCOUT-O3 and TWP-ICE and thus served as an important complement to both programs. ACTIVE focused particularly on the measurement of a variety of chemical species, including aerosols (Allen et al. 2008). The aerosol component of ACTIVE was partly motivated by the outcome of the second phase of the EMERALD (Egrett Microphysics Experiment with RAdiation Lidar and Dynamics, Whiteway et al. 2004) program, which provided a unique view of the anatomy of cirrus outflow from Hector thunderstorms. Aerosols were not targeted during this program while they strongly affect the dynamical and microphysical structure of cirrus clouds (e.g. Connolly et al. 2006).

ACTIVE was aimed at determining the impact of deep convection on the composition of the UT/LS region and its relative importance compared with large-scale ascent. During the first phase of ACTIVE, which was held concurrently with SCOUT-O3, the emphasis was put on studying

isolated thunderstorms. The IOP was conducted from November 7 to December 9, 2005 over the Tiwi Islands during the buildup of the summer monsoon. Vaughan et al. (2008) described the science objectives and the design of the IOP. A range of observational equipment was deployed during this IOP including several research aircrafts, radiosondes and precipitation radars, such as the BMRC/NCAR C-POL radar (Keenan et al. 1998). This dataset has provided significant insights into the onset and development of isolated thunderstorms over northern Australia.

Though these observational studies are crucial information sources to clarify the processes involved in UT/LS exchanges, measurements cannot provide a complete picture of the evolution of the 3D structure of deep convective events. In this context, high-resolution cloud-resolving models have been a helpful tool to refine and quantify these processes, and to confirm results from observations. In support of observational studies of isolated island thunderstorms, only a few numerical studies were performed. To our knowledge, the first ones were conducted by Golding (1993) using the UK Met Office UM (Unified Model, Golding 1992) at 3-km horizontal resolution to examine two days from the ITEX field campaign. Using a simplified initialization from soundings, the simulations were able to reproduce successfully the development of deep convection over the Tiwi Islands. Convection was found to be first initiated where the convergence of sea-breeze flows was maximum, due to the shape of the coastline. The timing, strength, and location of convection were predominantly determined by the convective available potential energy (CAPE), given sufficient heating. Saito et al. (2001) investigated an observed case from MCTEX using MRI NHM (the Japanese Meteorological Research Institute Non Hydrostatic Model, Saito and Kato 1999) at 1-km horizontal resolution. Good agreement was obtained between the simulated and observed developments of Hector. The sensitivity of the development of deep convection to microphysics, and topography and size of the islands was also examined. Crook (2001) performed

idealized simulations of Hector using both linear and nonlinear models. The effects of low-level wind, CAPE, and sensible and latent heat fluxes on the strength and location of convection were investigated. Consistent with observations, it was found that major convection occurs along the downwind side of the islands and that the intensity of Hector storms increases when the direction of the low-level flow turns towards the major (i.e. longer) axis of the islands.

The predictable and isolated nature of Hector thunderstorms makes them ideal case studies for evaluating numerical models. It is noteworthy that, apart from the simulation by Saito et al. (2001), there is no realistic simulation published in the literature. Saito et al. (2001) used a 1-km horizontal resolution, which is likely to be insufficient to resolve faithfully the basic thunderstorm structure (e.g. Bryan et al. 2003). Furthermore, the impact of deep convection on the composition of the TTL was not investigated.

In the present paper, we discuss results from the ARW (Advanced Research core of the Weather Research and Forecasting (WRF) model, Skamarock et al. 2007) and UK Met Office UM (Davies et al. 2005) models for the golden day during the first phase of ACTIVE, that is November 30, 2005, for which a severe Hector thunderstorm developed. These two models are representative of the next generation of numerical weather prediction models and both of them have already been applied to tropical area. Using two models is expected to lead to more robust conclusions and to provide eventually deeper insights in the processes under investigation. High-resolution cloud-resolving simulations have been performed using a horizontal resolution as fine as 250 m. The setup of the models is presented in § 2. The strategy for evaluation of the models is discussed as well. The large-scale environmental flow over northern Australia during the Hector episode is described in § 3. Four main phases have been identified in the development of the Hector thunderstorm during this episode, namely: *Onset*, *Triggering*, *Hector*, and *Dissipation*.

These phases are detailed in light of results of the ARW and UM models in § 4. The impact of convective overshooting on the redistribution of atmospheric constituents within the UT/LS is discussed in § 5. In particular, we focus on the understanding and quantification of the imprint of Hector onto the water content in the LS. Finally, a summary and concluding remarks are given in § 6.

2. Setup of the ARW and UM models

The ARW and UM models were used to investigate the dynamics of a severe Hector thunderstorm over the Tiwi Islands. The Tiwi Islands consist of a pair of closely spaced islands (Bathurst Island and Melville Island) separated from each other by a narrow tidal channel (Apsley Strait). This group of islands is about 100-km long and 75-km wide. The orography of the islands is quite gentle (see Figure 1). The ridge to the south of Melville Island reaches only height up to about 120 m above mean sea level (a.m.s.l.). The terrain slopes gently down to the sea with shallow tributary valleys. Vegetation is mainly composed of open forests and grasslands and is not dense because of the traditional indigenous land management practices. Indeed, vegetation is burnt during the dry season in order to prevent fire outbreaks from developing and to preserve grasslands for hunting. FIG. 1

a. Downscaling and grid set-up

The two models were run on multiple grids using one-way nests. Table 1 gives the spatial coverage and the horizontal resolution of the grids used for the simulations. The domains using a 1-km horizontal resolution (ARW3 and UM3) are displayed in Figure 1. The ARW model was run down to a horizontal resolution as fine as 250 m to investigate the sensitivity of the

results to horizontal resolution. The motivation is that a 1-km horizontal resolution might be too coarse to faithfully represent physical processes of cloud turbulence that occur in deep convection (see Bryan et al. 2003, for a guide to resolution requirements for the simulation of deep moist convection). For that specific run at high resolution, 621 E-W by 621 N-S grid points were used to cover a domain over the islands (see Figure 1). The computations with ARW were made on 115 vertical levels up to 3 hPa. The grid was stretched along the vertical axis to yield an averaged vertical grid spacing of 500 m and to accommodate a high resolution ($\sim$ 100 m on average) both close to the ground surface and within the UT/LS region. The spatial resolution within the UT/LS region needs to be fine enough to resolve a range of convective structures and to reduce artificial gravity wave damping. A vertical resolution of the order of 100 m is very likely to be sufficient to resolve the short vertical wavelengths of the gravity waves induced by deep convection in the Darwin area. Indeed, these wavelengths were observed to be typically in the order of a few kilometers (e.g. Tsuda et al. 2004). Two distributions of vertical grid spacings were employed for the UM runs. For the grids with a horizontal resolution larger than 1 km, we used 38 vertical levels, with a top at 1 hPa. The vertical grid spacing was in the order of 1000 m within the UT/LS region. As for the run with a 1-km horizontal resolution, 76 levels were used and the vertical grid spacings were reduced by half. Table 1

The topography of the Tiwi Islands is basically flat (see Figure 1). Nonetheless the ridge to the south of Melville Island may have an impact on the timing, structure, and strength of deep convection. Saito et al. (2001) found that the development of Hector tends to be delayed and the maximum vertical velocity becomes smaller when the topography is flattened. Hence, a high-resolution topography would be required to simulate accurately Hector events. In our ARW runs we used digital elevation data from the Shuttle Radar Topography Mission (SRTM, Farr et al.

2007) at ~ 90-m resolution. As for the landcover, we used the MODIS MOD12 land cover product at 1 km resolution (Friedl et al. 2002) for the domains ARW3 and ARW4 and remapped it to the USGS classification implemented in ARW. For the other domains and the other characteristics of the soil and the ground surface (such as soil type, monthly surface albedo), static data were derived from the default geographical data that are provided with the WRF preprocessing system. As for the UM, vegetation and soil types were extracted from the AVHRR IGBP dataset (Loveland et al. 2000). Orography was processed from the GLOBE dataset (Hastings and Dunbar 1998), except for the finer-resolved domain (UM3), for which the SRTM dataset was used (as for ARW). Both the AVHRR IGBP and GLOBE datasets are available at 1-km resolution. Other soil and ground surface data were specified from climatological values.

Initial and lateral boundary conditions of the coarser domain ARW1 were derived from the ECMWF (European Centre for Medium-range Weather Forecasts) gridded analyses available every 6 h with a horizontal resolution of $0.5°$ on operational pressure levels up to 3 hPa for vertically distributed data, and surface and soil levels for surface and deep-soil data. As for the UM, the global run was initialized by a data-assimilated global dump provided by the UK Met Office. A grid nudging technique (see for instance Stauffer and Seaman 1990) was employed for the coarser domain ARW1 during the first 6 h in order to shorten the spin up time. No nudging was performed in the UM simulation. A relaxation zone covering a few grid cells around each domain (5 in ARW and 12 in UM) was employed to smooth gradients near the lateral boundaries. In our work, we focus on the Hector storm that developed in the afternoon on November 30, 2005. A tropopause fold passed over the simulated domains from November 23 to 27, 2005, irreversibly mixing stratospheric air into the troposphere. As a result, the troposphere was very dry in the range 200–600 hPa. This persistent dry layer prevented convection from developing over land,

reducing cloud cover (to about 10 %) and precipitation (to about 50 mm a day) over the area of interest. Hector storms developed in the afternoon on November 27 to 30, 2005. We found that starting the ARW simulation on any of these days does not change much the timing, structure, and strength of Hector on November 30, 2005. However, it does have a significant impact on the water content in the UT/LS. This is shown in § 5.c. Basically, we found that starting the simulation on November 28, 2005, gives the best set of results when compared with observations and that starting it later on in time may give misleading results. Therefore only the results from the ARW simulation starting on November 28, 2005, are presented thereafter. As for UM, the simulation was started on November 29, 2005, at 1200 UTC, since starting it on November 28, 2005, would lower its forecasting skill considerably.

b. Parameterization of physical processes

For the simulations using a horizontal resolution down to 1 km, sub-grid scale (SGS) mixing was classically parameterized within the boundary layer physics. We used the YSU (Hong et al. 2006) and operational (Lock et al. 2000) boundary-layer parameterization schemes in ARW and UM, respectively. Both schemes are non-local and take explicitly into account entrainment at the top of the boundary layer. These schemes assume that there is a clear scale separation between the sub-grid and resolved scales, so that they can be treated independently. This assumption is less clear as grid sizes approach a few hundred meters or less. In these cases, the schemes should be replaced by a fully 3D local SGS scheme, and such simulation is referred to as large-eddy simulation (LES).

The LES capability of ARW was not applicable to real cases in its current release (version

2.2). As a matter of fact, the SGS scheme was not coupled with the surface fluxes, which are calculated by the soil-vegetation model. For the finer-resolved domain (ARW4) using a horizontal resolution of 250 m, we recoupled these fluxes and included them in the buoyancy and shear production terms of the turbulent kinetic energy equation (E. D. Grell, personal communication). Note that we used the level-1.5 sub-grid scale scheme by Deardorff (1980).

The classical Monin-Obukhov surface layer scheme was used to provide surface forcing in terms of momentum, heat, and moisture fluxes. The land-surface energy budget was calculated by the Noah soil-vegetation model (Ek et al. 2003) in ARW and by the Met. Office Surface Exchange Scheme (MOSES, Essery et al. 2003) in UM. The radiation schemes provide surface downward long-wave (LW) and short-wave (SW) radiation for the land-surface energy budget as well as atmospheric heating due to radiative flux divergence. In ARW, we used the CAM3 radiation package (Collins et al. 2006). As for the UM, the Edwards-Slingo radiation scheme (Edwards and Slingo 1996) was employed. Both schemes include a multi-band calculation of atmospheric heating for both the LW and SW streams.

For the coarser grids with a horizontal resolution larger than 4 km, SGS effects of convective and shallow clouds were parameterized by a mass-flux-based cumulus scheme. We used the ensemble cumulus scheme introduced by Grell and Dévényi (2002) in ARW and a scheme based on the Gregory and Rowntree (1990) cumulus scheme in UM. Note that the latter scheme had numerous enhancements to the original scheme since (in particular, separate updraught and downdraught parameterization, convective momentum transport, and CAPE closure). For the finer-resolved grids with a horizontal resolution of 1 km and less, convection was explicitly resolved and the cumulus scheme was switched off. We used the microphysical schemes by Thompson et al. (2004, 2006) and Wilson and Ballard (1999) in ARW and UM, respectively. The Thompson

scheme has six classes of hydrometeors, namely water vapor, cloud liquid water, rain, cloud ice, snow and graupel. In addition, the number concentration of cloud ice is predicted as is the case in double-moment schemes. As for the version of the Wilson and Ballard scheme that we used, it has prognostic water vapor, cloud liquid water, rain, total ice (ice and snow), and graupel.

c. Strategy for evaluation of the models

The models were evaluated using observational data from the IOP. Results of the simulations at 1-km horizontal resolution were compared with both ground surface and vertically-distributed measurements. In the present study, the strategy for evaluation of the models and further analysis has to select the most appropriate variables to optimally characterize the key flow features and physical processes. Hereafter, we decided to use the following variables: vertical velocity, sensible heat flux, precipitation rate, and water mixing ratios.

The nominal boundaries of the TTL region can be defined in several different ways based either on the thermal or dynamical structure of the region. A dynamical definition of the TTL using particular values of potential vorticity (PV) might not be appropriate over the Tropics where PV becomes ill conditioned (see for instance Gettelman and Sobel 2000). The definition adopted in our work is based on the thermal structure of the UT/LS region. Convenient boundaries for the TTL are the potential temperature lapse rate minimum at about 11 km in altitude (~ 345 K in isentropic coordinates) and the cold point tropopause at about 17 km (~ 370 K). The main focus of our study is whether and how deep convection affects the water content in the UT/LS. Hence, an important boundary that occurs within the TTL is the LZH at about 15 km (~ 355 K). Indeed, only convection that reaches this level facilitates the ascent of air into the LS. Therefore, the LZH

is used as the lower boundary of the TTL (as in Sherwood and Dessler 2000) and termed the TTL height thereafter.

The minimum time period at which the results needs to be output to capture the non-stationary structure of deep convection should be smaller than the typical overturning time scale τ of strong updraughts. Let us assume that the typical vertical extension h of strong updraughts is in the order of the TTL height (15 km) and that their maximum vertical velocity $w_\star$ is about 25 m s^{-1} (see § 4.b). This yields $\tau \equiv h/w_\star = 10$ min. Hence we fixed the frequency of the outputs to 10 min.

3. Large-scale environmental flow

The synoptic condition over the Maritime Continent, and in particular over northern Australia, is mainly driven by the monsoon trough (e.g. McBride 1987). When the wind regimes from the northern and southern hemispheres are well distant from the equator, the ITCZ (Inter Tropical Convergence Zone) forms a monsoon trough. Basically, the trough lies north of Australia during the Australian summer monsoon. The air converges over the Maritime Continent (Ramage 1968), which is dominated by low level westerly flow and upper level easterly flow. During the IOP, the onset of the monsoon started on December 26, 2005. The preceding period may be considered as a buildup period. During the buildup of the monsoon, the environmental flow is usually dominated by easterly flow (e.g. Keenan and Carbone 1992; Kullgren and Kim 2006). Low level winds with a westerly zonal component were not often observed during the IOP. A low level north westerly flow was observed on November 30, 2005, the flow above being westerly up to about 12 km and easterly aloft (see Figure 2). As suggested for instance by Crook (2001), this synoptic pattern favors the triggering of Hector thunderstorms. Indeed, deep convection is initiated as a result of

convergence of sea-breeze flows and its intensity is maximum when the low-level flow is along the major axis of the islands. The timing and structure of the sea breeze flows is detailed in § 4.

A severe Hector thunderstorm started to develop on November 30, 2005 at about 1400 LT (Local Time $=$ UTC$+9.5$). The initiation of deep convection requires conditional instability and a trigger mechanism, which is discussed in § 4. During MCTEX, Keenan et al. (1990) found that thunderstorms develop in an environment with low shear, moderate CAPE (in the order of 1500 J kg^{-1}), and high moisture. In our case, at 1430 LT the convective inhibition was rather weak and the CAPE was very large (~ 3464 J kg^{-1}, see Figure 2). The precipitable water was found to be 5.0 cm, which value is close to that observed during MCTEX (4.7 cm). FIG. 2

Figure 3 shows MTSAT-1R satellite images over northern Australia every 6 h from 1000 LT to 2200 LT. Prior to deep convection this region did not experience high clouds (see Figure 3(*a*) at 1000 LT). By early afternoon deep convective clouds extended over the area of Darwin and the south-east coast of Melville Island. As from about 1500 LT to 1600 LT, deep convective storms intensified (see Figure 3(*b*) at 1600 LT) and produced heavy precipitation. Thunderstorms lasted for about two hours. At the end of the afternoon high clouds spread all over the islands. By early evening the convective system dissipated. Finally, in the evening remaining clouds had moved off the islands (see Figure 3(*c*) at 2200 LT). FIG. 3

4. Structure of the Hector thunderstorm

a. Horizontal structure

During the morning hours, the boundary layer grows rapidly as a result of ground surface

heating, reaching a height z_i of about 2000 m by early afternoon. The air originating from the westerly flow above the low level north westerly flow is entrained into the mixed layer once the low level flow encroaches on the layer of westerly flow, which is located at about 1000 m (see Figure 2). Later on in the afternoon, the height of the boundary layer is more difficult to define. As Hector develops, deep convective cells strongly modify the structure of the boundary layer. Basically, the depth of the mixed layer may be either shallow or deep depending on the location and strength of the convective cells. In this case, the boundary-layer height is a quantity that is not really appropriate to characterize the deep convective cells.

The large-scale environmental flow affect the timing, structure and strength of the atmospheric circulation over the islands as discussed for instance by Crook (2001). Nonetheless, thunderstorms develop almost every afternoon during the pre-monsoon season. The lifecycle of the observed Hector storm is described in the following. Sea-breeze fronts form all along the coastline as a result of the temperature gradient between the ocean and the land. This is the *Onset* stage. The inflow depth was about 800 m and lay between the mixed-layer depths over the ocean and over the land. This result is consistent with the findings of Oliphant et al. (2001) and Schafer et al. (2001) during MCTEX though being shallower by a few hundred meters (depths averaged 1200 m). The north westerly low level flow led to conditions which were particularly favorable for convective initiation. Indeed, the low-level flow was almost along the major axis of the islands. Hence, the convergence of the sea-breeze flow is intensified (see also Liu and Moncrieff 1996; Carbone et al. 2000; Crook 2001; Wilson et al. 2001). The air is thus more likely to be lifted to the level of free convection. Note that enhanced convergence may also occur as a result of either gust or cold or dry fronts, or be induced by topographic features (Kingsmill 1995).

Sea-breeze flows first develop around 1300 LT along the windward coast north of the islands

and propagate more rapidly than along the leeward coast. Indeed, along the south coast the sea-breeze front opposes the low level flow. Thus, the progression of the sea-breeze front is slowed down and the air is lifted further up. At that stage (thereafter referred to as *Triggering*), the convective activity over the interior of the islands is still typical of that of the convective boundary layer. Shallow clouds form at the top of the boundary layer and spread over the islands. Maximum temperature and minimum pressure take place over the center of the islands defining a heat low that cause island-scale convergence (see also Skinner and Tapper 1994).

As from about 1400 LT, sea-breeze flows penetrate inland rather rapidly (within one hour or so) and converge over the center of the islands (see Figures 4(*a*) and 4(*b*)). Thunderstorms develop along the convergence line north of the ridge to the south of Melville Island. Though the ridge reaches only height up to about 120 m, the topography has a significant impact on the atmospheric circulations and consequently on the characteristics of the storm. The elevation associated with the escarpment makes the ridge a region of maximum heating along the convergence line and thus a preferred region of storm genesis. By 1500 LT, the sea-breeze flows have penetrated to the center of the island and reach their maximum strength. At that time, vertical velocities close to the ground surface are maximum and exceed 1 m s^{-1} (see Figures 4(*c*) and 4(*d*)). This is the *Hector* stage.

By 1530 LT, the air temperature in the center of the islands has dropped by about 3–5 °C as a result of the development of cold pools from thunderstorm outflows. At the same time the surface water vapor mixing ratio has increased because of the heavy rainfall. Radially spreading cold pools force air to rise, generating new convective cells, which in turn generate cold pools. At that stage, convection is self-sustained and free from the sea-breeze fronts. As Hector develops, the strength of the sea-breeze flows is dampened rapidly by the thunderstorm outflows.

FIG. 4

Sea-breeze flows all along the coastlines have significantly decreased in intensity by 1600 LT and an off-shore flow develops as cold air induced by the storms spread out (see Figures 4(*e*) and 4(*f*)). As the storms spread out horizontally at the surface over the center of the islands, gust fronts travelling offshore develop occasionally. The gust fronts can force warm air to rise and locally lead to the development of clouds along the coastlines (as illustrated in Figure 8(*b*)). By 1700 LT, the storm is moving downstream westwards, similarly to convection bands during the monsoon (e.g. Keenan and Brody 1988) and dissipates (see Figures 4(*g*) and 4(*h*)). The *Dissipation* stage lasts for about two hours. Later on, the oceanic boundary layer air is advected over the islands and resets the timing and structure of the Hector convective system.

It is noteworthy that the values of sensible heat flux obtained with ARW and UM can differ by up to 20–30 %. This can be explained by different soil and ground surface characteristics (as mentioned in § 2.a.) as well as a more extensive cloud cover simulated by UM. One might expect the structure and strength of Hector to be different in both runs. Indeed, the development of deep convection depends on the surface heat fluxes since they warm, mix, and moisten the boundary layer, which needs to contain sufficient moisture to support deep convection as well as precipitation. Interestingly, both models reproduce the development of Hector fairly well. Consistent with this result, Simpson et al. (1993) found that the islands still provided sufficient surface heat fluxes to initiate convection on a day when the islands were under a dense cirrus overcast. This would mean that the intensity of Hector storms could not be controlled only by the surface heat fluxes. Robinson et al. (2008) suggested that the spatial extent of ground surface heating can control the intensity of Hector. The authors argued that deep convection is stronger when the vertical to horizontal aspect ratio of the thermally-driven boundary layer is equal to the ratio of the vertical wavelength to horizontal wavelength of propagating internal gravity waves.

FIG. 5

The early stages of the development of Hector (*Onset* and *Triggering*) show very little convective precipitation. Initially, the storm has characteristics of non squall multicellular convection (i.e. convective cells separated by stratiform regions). The convective regions are characterized by large vertical velocities greater than the typical fall speed of hydrometeors (i.e. about 2–3 m s^{-1}). The convective cells propagate in a discrete way and are persistent in a sense that at least one cell is active. As for the stratiform regions, they are characterized by vertical velocities that are much less than the typical fall speed of hydrometeors. In that case, ice particles within the upper layers of clouds fall while growing (see for instance Steiner et al. 1995).

Thunderstorms are first initiated to the east of Melville Island and then move westwards (see also Keenan et al. 1994; Carbone et al. 2000). During the mature stage of *Hector* (see Figure 6), the convective activity over the islands increases rapidly. The merging of active convective cells leads to a rapid development of the Hector thunderstorm. The convective complex organizes along a East-West line over the center of the islands. The most intense precipitation is associated with this period of explosive convection, with precipitation rates locally as large as 100 mm h^{-1}. Later on, when the developing cold pool generated by thunderstorm outflows encompasses most of the islands, a reorientation of the convective system to a North-South line perpendicular to the environmental shear is observed. The storm then moves westwards with a squall-like structure (i.e. convective front with a trailing stratiform region). In the *Dissipation* stage, stratiform precipitation becomes prevalent and moves off the islands westwards. To complement the qualitative comparison of the spatial distribution of rainfall rate in Figure 6, the performance of the models has been further quantified by a statistical comparison of the rainfall rate over the domain ARW4. Hourly-accumulated precipitation generated by ARW and UM every hour from 1230 LT to 2130 LT has been compared with that from the BMRC/NCAR C-POL radar measurements.

The normalized mean bias is -21.15 % for ARW and -51.62 % for UM. FIG. 6

b. Vertical structure

The initial convection during the *Triggering* stage is rather shallow with cloud tops in the range 8-10 km. Upward motion in some clouds reaches 8–10 m s^{-1} and precipitation starts. After that the development of Hector has a stepwise character as storm cells merge to form tall hot towers. The duration of this intense convection is in the order of one hour. A convective complex with an extensive anvil cloud develops in the mature phase, producing heavy rainfall. Note that mergers represent only about 10 % of the convective systems while producing about 90 % of the rainfall over the islands (Simpson et al. 1993). In Figure 7, the vertical distribution of microphysical variables simulated by the models at 1600 LT is compared with the classification of hydrometeors from the BMRC/NCAR C-POL radar measurements at 1430 LT. The measurements were processed by the Bureau of Meteorology, Australia, to create horizontal cross-sections at different altitudes. Note that the time for comparison is not identical. Indeed, for the comparison to be qualitatively fair, we had to select a time for which the radar scanned an active convective cell. Cloud-top height reaches 17 km and an anvil develops at the top of the convective complex. The maximum vertical velocity is located around 10–12 km and exceeds 22 m s^{-1}. Note that the maximum simulated values over the inner domains ARW3 and UM3 reach 30–40 m s^{-1} (not shown). This is consistent with the continuous measurements at Darwin, Australia, discussed by May and Rajopadhyaya (1999), for which the most intense updraughts occur above the melting level (at about 5 km in altitude). Hydrometeors are produced and uplifted by deep convection. Within updraughts exceeding several meters per second, upper-level hydrometeors grow rapidly by riming

(liquid water freezing onto ice crystals). Graupel (ice crystals that undergo extensive riming) is found between the melting level and the LZH (at about 15 km in altitude), and either falls out or provides nuclei for hail. Note that in the simulations performed with ARW, hail is not discriminated from graupel. The melting level is easy to identify in Figure 7(*a*) as it is known to give a bright band of reflectivity in the stratiform cloud layers and hence a discontinuity in the class of hydrometeors. While falling out, hydrometeors grow by vapor diffusion and precipitate out below the melting level. Rain eventually occurs and a downdraught forms all around the updraught while creating a cold pool at the ground surface.

The remaining hydrometeors that do not fall out are mainly composed of snow and ice crystals above the freezing level. These hydrometeors are subjected to weaker vertical motions and remain aloft to form an anvil, which can be either advected or left decaying. The strong updraught displayed in Figure 7 does overshoot its level of neutral buoyancy. In that case, rather small ice particles are lifted higher up and spread out. The persistence of the anvil as well as the injection of small ice particles above the tropopause can lead to changes in the radiative balance in the atmosphere and either a dehydration or a moistening of the LS. Elements of quantification of such impacts are proposed in § 5.

FIG. 7

c. Sensitivity to horizontal resolution

To assess the impact of refining horizontal resolution on the development of Hector we compared results of the simulations performed with ARW using horizontal resolutions of 1 km (domain ARW3) and 250 m (domain ARW4). Figure 8 shows the *Hector* stage at 1600 LT as simulated over the domain ARW4. Basically the features of the storm do not change much and the

flow structure is much more detailed when increasing horizontal resolution. As expected, the higher-resolution simulation better resolves the convection. The normalized mean bias for hourly-accumulated precipitation is 15 %. This represents an improvement on the coarser resolution simulation, for which the normalized mean bias was -21.15 %.

The low level north westerly flow imposes an onshore flow along the windward coast north of the islands and an offshore flow along the south coast. The onshore flow facilitates the inland penetration of the sea-breeze front. Conversely, the offshore flow results in a sharp front close to the coastline. This explains that Hector first developed along the leeward coast since the front is likely to produce greater lifting. Horizontal convective rolls (see Etling and Brown 1993, for a review) perpendicular to the sea-breeze fronts develop over the clear-sky areas. This feature is illustrated in Figure 8(*a*) and was not so clear in the 1-km horizontal resolution simulations. Note that horizontal convective rolls were also suggested by Saito et al. (2001) during MCTEX. The wavelength that is associated with the horizontal convective rolls is in the order of 3–4 km. This value is in good agreement with the theoretical wavelength $\ell = 2\sqrt{2}\, z_i$ determined by Kuettner (1971), yielding a roll aspect ratio of about 2.8. As discussed in § 4.a, the boundary-layer height z_i is a quantity that is not really appropriate during the *Triggering* and *Hector* stages but prior to convection z_i was typically in the order of 2 km, giving $\ell \sim 5$ km. These rolls develop in an environment with sufficient speed shear (see for instance Etling and Brown 1993) and tend to be aligned parallel to the vertical wind shear vector. A low speed shear environment usually produces cellular convection close to that observed in the simulations at 1-km horizontal resolution. The fact that horizontal convective rolls are not recognizable using a horizontal resolution of 1 km is certainly due to a too coarse horizontal resolution. Indeed, a high horizontal resolution being 500 m or less is necessary to produce horizontal convective rolls (e.g. Balaji and Clark 1988).

As discussed in great detail by Dailey and Fovell (1999), the interaction of the sea-breeze front with these rolls produces spatial variation in the sea-breeze front and can provide sufficient lifting to initiate deep convection. Indeed, lifting is enhanced at frontal locations where roll updraughts intersect. The enhanced convection induces subsidence above the roll downdraught intersections that generates a positive convective feedback helping to maintain convection. The same mechanism do exist along the convergence line in Figure 8(*a*) where along-line vertical velocity maxima enhance deep convection. A similar mechanism was observed by Wilson et al. (1992) at the intersection of a convergence line with horizontal convective rolls near Denver, Colorado, USA. The results of the simulation usin a 250-m horizontal resolution suggest that this mechanism might play an important role in modulating convection in the frontal environment over the islands. However, one need to bear in mind that the situation can be much more complicated when the sea-breeze front and the environmental low level flow are not aligned (see for instance Fovell and Dailey 2001).

FIG. 8

5. Imprint of Hector onto stratospheric water vapor

It is widely accepted that overshooting convection does occasionally penetrate the TTL up to the cold point (e.g. Liu and Zipser 2005) as is the case in Figure 7 for instance. There has been considerable discussion over the years as to whether a significant amount of tropospheric air is injected into the stratosphere by deep convection at the global scale. Understanding whether and how overshooting convection affects the water content in the UT/LS region is particularly important since water vapor does have a significant impact on the radiative balance of the atmosphere as a greenhouse gas, and hence on climate.

a. Review of our current understanding

The extreme dryness of the stratosphere prevailed on Brewer (1949) to suggest that air enters the stratosphere primarily in the Tropics, where it is dried by condensation. Newell and Gould-Stewart (1981) narrowed down this tropical region where the tropical tropopause is cold enough to dehydrate the air entering the stratosphere to account for the low water vapor mixing ratio. The authors referred to this temporally and spatially limited region as the stratospheric fountain, which included the western tropical Pacific, northern Australia, Indonesia and Malaysia during the November–March period and the Bay of Bengal and India during the monsoon season. However, it turned out that the stratospheric fountain hypothesis is not necessary since Mote et al. (1996) and Dessler (1998) showed that the temporal and spatial restrictions, respectively, do not hold. Hence, air can enter the stratosphere at any time and any longitude in the Tropics rather than at preferred locations and times. Zhou et al. (2001) examined an extended version of the radiosonde dataset used by Dessler (1998) and found a cooling trend in the mean tropical tropopause temperature and a long-term increase in stratospheric water vapor. This long-term increase is significantly larger than the one expected from oxidation of increased methane (Gettelman et al. 2000), indicating that the stratospheric fountain might still be necessary. Fueglistaler and Haynes (2005) found no cutting-edge evidence in 40 years of ECMWF reanalyses that explains the long-term increase in stratospheric water vapor. This suggests that dynamical pathways and the tropopause temperature might not be the only important factors controlling water vapor in the LS. Hence, it is difficult to account for the extreme dryness of the stratosphere unless tropical regions determine the dehydration of the air entering the stratosphere. The role of tropical convection in UT/LS exchanges is not well understood but deep convection eventually provides an alternative pathway for regulating

the water content in the UT/LS region.

The regulation of the water content in the UT/LS by deep convection results from a combination of several processes. These processes are briefly summarized in the following. A large-scale ascent from the UT to the LS is expected above the LZH, where the clear sky mass flux is upward (e.g. Highwood and Hoskins 1998). This process does not require convection to overshoot the tropopause. Horizontal transport through the cold trap regions then causes air reaching the tropopause elsewhere to be dehydrated to the low saturation mixing ratios characteristic of the tropical tropopause (Holton and Gettelman 2001). Overshooting deep cumulus clouds do occasionally penetrate the tropopause up to the cold point (Liu and Zipser 2005). These events do not support a permanent vertical transport, but a temporally and spatially localized one. Since deep convective structures overshooting their level of neutral buoyancy are colder than their environment, air can be dehydrated rapidly (e.g. Danielsen 1982; Kley et al. 1982; Danielsen 1993; Sherwood and Dessler 2000, 2001). As the air rises in deep convective turrets it is cooled, and water vapor is frozen out. Most of the ice particles are removed by sedimentation, and thus dehydrate the air. However, if ice particles do not settle out and remain in the LS the air is moistened as ice particles evaporate (Vömel et al. 1995; Grosvenor et al. 2007). There are other processes such as optically thin cirrus (Jensen et al. 2001) and internal gravity waves (Potter and Holton 1995; Teitelbaum et al. 2000) which may contribute to the dehydration of the LS. The relative importance of these processes in regulating the water content in the UT/LS region is still uncertain (e.g. Holton et al. 1995). Gettelman and Birner (2007) argued, based on the results of global-scale simulations, that large-scale processes, and the large-scale effects of small-scale processes, are the ones that are globally controlling the variability of the TTL. While the details of small-scale processes in these simulations may not be important for the climatology of the TTL, the authors indicated that

further investigation is needed to understand the role of cloud processes and whether models are providing a correct picture of the TTL for the right reasons.

b. Total water observations above Hector

Total water (water vapor and ice) was measured by a fast in-situ stratospheric hygrometer (FISH, Zöger et al. 1999) on board of the M55-Geophysica research aircraft during the ACTIVE/SCOUT-O3 field campaign. The FISH measurements provided invaluable information on the vertical distribution of total water above and around Hector. Unfortunately, the aircraft cannot fly into the updraughts and convective overshoots. Hence, the measurements have to be considered as representative of an overall signature of Hector, for which the most extreme values are discarded. Figure 9 shows two vertical distributions of total water obtained from flight tracks on November 19 and 30, 2005, from 1255 LT to 1712 LT and from 1300 LT to 1721 LT, respectively. The flight track on November 30, 2005, from 1500 LT to 1700 LT is displayed in Figures 6(*a*) and 6(*b*). Note that the virtual potential temperature θ is used as the vertical coordinate.

FIG. 9

Hector did not develop on November 19, so that the corresponding vertical distribution may be regarded as a typical background profile. The mean water vapor mixing ratio at 380 K is about 2.5 ppmv, which value is close to the one found by Kelly et al. (1993) over Darwin, Australia, during the STEP tropical mission in 1987 (values averaged 2.4 ppmv at 375 K). The imprint of the Hector event on November 30 onto the water content in the UT/LS region appears clearly when superimposed on the background profile. Within the TTL, total water mixing ratios as high as 100–200 ppmv were observed. The region of minimum water vapor (often referred to

as hygropause) lies well above the TTL at around 380–390 K. The elevated hygropause may be regarded as a manifestation of the seasonal cycle in tropopause temperature (Mote et al. 1996). Teitelbaum et al. (2000) provided an alternative explanation based on an uplift of the tropopause during an intense convection event and a reestablishment of the temperature minimum at a lower altitude after the event while the hygropause remains elevated. Considerable amounts of ice are present above the hygropause, especially around 400 K and 420 K with values as large as 10–40 ppmv (Corti et al. 2008), for which total water RH_{ice} is greater than 150 % (see Figure 9). This ice must have been dropped off over there as a result of overshooting convection as we show in § 5.c. The presence of ice may lead to a dehydration or moistening of the LS via sedimentation or sublimation, respectively. There is observational evidence that the water vapor was subsaturated with respect to ice in the LS on that day (Corti et al. 2008) and therefore the presence of ice would lead to a moistening of the LS. The size distribution of ice particles and the water vapor mixing ratio are key to determining the potential for either dehydration or moistening. Smaller particles fall out more slowly than larger particles, allowing more ice evaporation while mixing with the surrounding air and eventually a moistening (or rehydration) of the LS. Larger particles sediment out more rapidly, allowing ice to be removed and a dehydration of the air. A major question that we cannot answer at that time (from the measurements presented herein) is the relationship between the overshooting air and the amount of small ice particles.

c. Simulated total water above Hector

There have been few high-resolution numerical studies on the role of overshooting tropical convection in regulating the water content in the UT/LS region. Küpper et al. (2004) investigated

a case using a cloud-resolving model run to equilibrium. The results showed no dehydration and that the non-convective fluxes of mass and water were predominant when compared with the corresponding convective fluxes. However, the model did not produce overshoots penetrating above the cold point, so that the effect of the most vigorous overshooting events was not represented. In a real case numerical study, Chaboureau et al. (2007) evidenced overshooting convection transporting mass and water vapor across the tropopause during the second TROCCINOX (TROpical Convection, CIrrus and Nitrogen OXides, Schumann 2005) field campaign, which took place in Brazil in early 2005. The simulated deep convective event was found to induce an upward transport of water vapor of a few tons per second across the tropopause. Consistent with this study, Grosvenor et al. (2007) found a significant moistening (up to 0.26 ppmv) of the LS by deep convection using idealized cloud-resolving simulations over the same area in Brazil during the HIBISCUS (Impact of tropical convection on the upper troposphere and lower stratosphere at global scale, Pommereau et al. 2007) IOP. In contrast to the cases studied by Chaboureau et al. (2007) and Grosvenor et al. (2007), Marécal et al. (2006) and Rivière et al. (2006) found a negligible impact of deep convection on the composition of the LS for an extreme event observed in February 2001 during the preparation campaign of the HIBISCUS IOP. Jensen et al. (2007) simulated overshooting convection in an idealized framework using a cloud-resolving model. The authors found no evidence that overshooting convection can dehydrate the TTL when it is initially ice subsaturated. Conversely, deep convection can dehydrate the LS if the TTL is initially supersaturated. Hence, the entry of water vapor in the LS depends on the TTL relative humidity (with respect to ice).

FIG. 10

The time evolution of the vertical distribution of total water as simulated by ARW and UM averaged over the domains ARW3 and UM3, respectively, is shown in Figure 10. Prior to Hector

(see Figures 10(*a*) and 10(*b*)), the vertical profile of total water is close to the background profile presented in Figure 9. The altitude of the hygropause is lower than observed and lies at about 370 K nearby the cold point. As Hector develops, the total water profile becomes multivalued, which indicates spatial variability and nonuniform ascent. During the mature stage of the storm (see Figures 10(*c*) and 10(*d*)), the total water mixing ratio exceeds a few tens of ppmv above the cold point. Total water RH_{ice} values greater than 150 % above the cold point confirm that overshoots contain more than enough ice particles that can either dehydrate or moisten the LS. As the preconvection water vapor in the LS was subsaturated with respect to ice (Corti et al. 2008), sublimation of the injected ice particles provides a source of water vapor. This condition is favorable for the air to moisten over the next few hours. The structure of the postconvection TTL after the *Dissipation* stage is dramatically different in the ARW and UM simulations (see Figures 10(*e*) to 10(*h*)). The TTL structure is not so much different during and after convection in the UM simulation. In the ARW simulation, the vertical distribution of total water reverts towards a distribution close to the preconvection one. The difference between the postconvection vertical distribution at 1830 LT (a couple of hours after Hector had formed) and that of the mature stage of Hector at 1530 LT (see Figure 11) suggests a moistening of the LS (above 380 K) up to 0.12 ppmv in the ARW simulation and up to 5.91 ppmv in the UM simulation. The moistening averages about 0.06 and 2.24 ppmv in the range 380–420 K for ARW and UM, respectively. The moistening derived from the UM simulation is much larger than that derived from the ARW simulation. The reason for this difference can be attributed to UM transporting more water vapor and ice in the LS than ARW (see Figures 10(*c*) to 10(*f*)). Further research is necessary to assess the primary causes of this difference between the two models. Maximum moistening is predicted below the LZH. However, it requires that this moist air is lofted across the tropopause via large-

scale upwelling to have an impact in the LS. If we start the ARW simulation on November 29, 2005 rather than on November 28, 2005, we found more moistening above 380 K (see Figure 11). This is consistent with the idea of the water vapor mixing ratio being driven to saturation more rapidly in the LS as Hector puts water one day after another. This buildup is likely to be an important factor when quantifying the water budget in the LS. FIG. 11

6. Summary and concluding remarks

The development of Hector on November 30, 2005 was simulated using the ARW (Advanced Research core of the Weather Research and Forecasting (WRF) model) and UK Met Office UM (Unified Model) cloud-resolving models. The simulations were performed with nests down to a horizontal resolution of 1 km. At this resolution, the timing, structure, and strength of deep convection were reproduced fairly well when compared with field campaign observations. The timing of this episode can be broken down into four main phases: *Onset* ($\sim$ 1100-1300 LT), *Triggering* ($\sim$ 1300-1500 LT), *Hector* ($\sim$ 1500-1700 LT), and *Dissipation* ($\sim$ 1700-1900 LT). These stages were described in great detail in § 4. We found that refining the horizontal resolution to 250 m with ARW leads to a better representation of convection with respect to rainfall. Horizontal convective rolls are produced at this horizontal resolution, while being not recognizable using a horizontal resolution of 1 km. The lifetime of Hector and its maximum height did not change much from the 1-km to 250-m horizontal resolution simulations, so that we might argue that a 1-km horizontal resolution is fine enough to simulate faithfully this Hector thunderstorm.

From our results, we clearly evidenced the intermittent penetration of overshooting convection through the isentropic barrier (~ 355 K), which lead to troposphere-stratosphere exchanges. In

particular, overshooting convection does affect the entry of water vapor in the LS. From a mechanistic point of view, tropospheric air crosses the tropopause by convective overshooting and then slowly rises as a result of radiative heating. This view is consistent with the parcel mixing model proposed by Sherwood and Dessler (2000, 2001). As stressed by Folkins et al. (2002), the potential for dehydration or moistening of the LS do exist provided that layers below overshooting convection detrain air within the TTL. In addition, only air detraining above the LZH is expected to affect significantly the water content in the UT/LS region. Convective ice lofting was found to be crucial in explaining the water content in the LS. Note that it was also found in previous studies to be essential in explaining the isotopic composition of the stratosphere (e.g. Keith 2000; Dessler et al. 2007). As the preconvection water vapor was ice subsaturated in the LS, we found a moistening rather than a dehydration of the LS. The moistening was found fairly significant above 380 K and averaged about 0.06 ppmv in the range 380–420 K for ARW. As for UM, the moistening was found much larger (about 2.24 ppmv in the range 380–420 K) than for ARW.

The question as to whether the rather infrequent overshoots within and above the TTL are sufficient to significantly affect the composition of the LS has not been addressed in the present study. This challenge requires a multi-scale approach from the global scale down to the cloud scale. Convective transport into the LS is certainly small compared with transport induced by larger-scale systems. Nevertheless, its efficiency in transporting quickly boundary-layer air makes it key to injecting short-lived species of tropospheric source (see for instance Dickerson et al. 1987) such as radon (e.g. Kritz et al. 1993) and some halogen compounds. More work needs to be done to quantify the relative importance of gradual versus episodic transport through the tropopause. Performing high-resolution simulations over a large domain of a few tens of thousands of square kilometers would be especially valuable for that purpose. We have left this point for

further research.

Acknowledgements. We appreciate the tremendous efforts of the ACTIVE/SCOUT-O3 PIs as well as all those who made the IOPs so successful. MRR and JAP acknowledge the UK Natural Environment Research Council (NERC) and the UK National Center for Atmospheric Science (NCAS) for funding as part of ACTIVE. MRR, JAP, and CS thank the European Commission for funding as part of SCOUT-O3. The Australian Bureau of Meteorology is acknowledged for having made the BMRC/NCAR C-POL radar data available for this work. CC would like to thank E. D. Grell for providing help with the implementation of the add-on LES module for ARW. The images of Figure 3 were derived from MTSAT-1R satellite imagery available from the Atmospheric Radiation Measurement (ARM) program archive. Time-consuming computations were performed thanks to the HECToR and HPCx UK national supercomputing facilities, which were accessed through NCAS. We wish to thank the UK Met Office and the NCAS Computational Modelling Services for helping on UM related issues.

REFERENCES

Allen, G., G. Vaughan, K. N. Bower, P. I. Williams, J. Crosier, M. Flynn, P. Connolly, J. F. Hamilton, J. D. Lee, J. E. Saxton, N. M. Watson, M. Gallagher, H. Coe, J. Allan, T. W. Choularton, and A. C. Lewis, 2008: Aerosol and trace-gas measurements in the Darwin area during the wet season. *J. Geophys. Res.*, **113**, D06306.

Atticks, M. G. and G. D. Robinson, 1983: Some features of the structure of the tropical tropopause. *Quart. J. Roy. Met. Soc.*, **109**, 295–308.

Balaji, V. and T. L. Clark, 1988: Scale selection in locally forced convective fields and the initiation of deep cumulus. *J. Atm. Sci.*, **45**, 3188–3211.

Brewer, A. W., 1949: Evidence for a world circulation provided by the measurements of helium and water vapour distribution in the stratosphere. *Quart. J. Roy. Met. Soc.*, **75**, 351–363.

Brier, G. W. and J. Simpson, 1969: Tropical cloudiness and rainfall related to pressure and tidal variations. *Quart. J. Roy. Met. Soc.*, **95**, 120–147.

Bryan, G. H., J. C. Wyngaard, and J. M. Fritsch, 2003: Resolution requirements for the simulation of deep moist convection. *Mon. Weath. Rev.*, **131**, 2394–2416.

Carbone, R. E., J. W. Wilson, T. D. Keenan, and J. M. Hacker, 2000: Tropical island convection in the absence of significant topography. Part I: Life cycle of diurnally forced convection. *Mon. Weath. Rev.*, **128**, 3459–3480.

Chaboureau, J.-P., J.-P. Cammas, J. Duron, P. J. Mascart, N. M. Sitnikov, and H.-J. Voessing, 2007: A numerical study of tropical cross-tropopause transport by convective overshoots. *Atmos. Chem. Phys.*, **7**, 1731–1740.

Chen, S. S. and R. A. Houze, Jr., 1997: Diurnal variation and life-cycle of deep convective systems over the tropical pacific warm pool. *Quart. J. Roy. Met. Soc.*, **123**, 357–388.

Collins, W. D., P. J. Rasch, B. A. Boville, J. J. Hack, J. R. McCaa, D. L. Williamson, B. P. Briegleb, C. M. Bitz, S.-J. Lin, and M. Zhang, 2006: The formulation and atmospheric simulation of the Community Atmosphere Model Version 3 (CAM3). *J. Climate*, **19**, 2144–2161.

Connolly, P. J., T. W. Choularton, M. W. Gallagher, K. N. Bower, M. J. Flynn, and J. A. Whiteway, 2006: Cloud-resolving simulations of intense tropical Hector thunderstorms: Implications for aerosol-cloud interactions. *Quart. J. Roy. Met. Soc.*, **132**, 3079–3106.

Corti, T., B. P. Luo, M. de Reus, D. Brunner, F. Cairo, M. J. Mahoney, G. Martucci, R. Matthey, V. Mitev, F. H. dos Santos, C. Schiller, G. Shur, N. M. Sitnikov, N. Spelten, H. J. Vössing, S. Borrmann, and T. Peter, 2008: Unprecedented evidence for overshooting convection hydrating the tropical stratosphere. *Geophys. Res. Lett.*, **35**, L10810.

Crook, N. A., 2001: Understanding Hector: the dynamics of island thunderstorms. *Mon. Weath. Rev.*, **129**, 1550–1563.

Dailey, P. S. and R. G. Fovell, 1999: Numerical simulation of the interaction between the sea-breeze front and horizontal convective rolls. Part I: Offshore ambient flow. *Mon. Weath. Rev.*, **127**, 858–878.

Danielsen, E. F., 1982: A dehydration mechanism for the stratosphere. *Geophys. Res. Lett.*, **6**, 605–608.

— 1993: In situ evidence of rapid, vertical, irreversible transport of lower tropospheric air into the lower tropical stratosphere by convective cloud turrets and by large-scale upwelling in tropical cyclones. *J. Geophys. Res.*, **98**, 8665–8681.

Davies, T., M. J. P. Cullen, A. J. Malcolm, M. H. Mawson, A. Staniforth, A. A. White, and N. Wood, 2005: A new dynamical core for the Met Office's global and regional modelling of the atmosphere. *Quart. J. Roy. Met. Soc.*, **131**, 1759–1782.

Deardorff, J. W., 1980: Stratocumulus-capped mixed layers derived from a three-dimensional model. *Boundary-Layer Meteorol.*, **18**, 495–527.

Dessler, A. E., 1998: A reexamination of the "stratospheric fountain" hypothesis. *Geophys. Res. Lett.*, **25**, 4165–4168.

— 2002: The effect of deep, tropical convection on the tropical tropopause layer. *J. Geophys. Res.*, **107**, D3/4033.

Dessler, A. E., T. F. Hanisco, and S. Fueglistaler, 2007: Effects of convective ice lofting on H_2O and HDO in the tropical tropopause layer. *J. Geophys. Res.*, **112**, D18309.

Dickerson, R. R., G. J. Huffman, W. T. Luke, L. J. Nunnermacker, K. E. Pickering, A. C. D. Leslie, C. G. Lindsey, W. G. N. Slinn, T. J. Kelly, P. H. Daum, A. C. Delany, J. P. Greenberg, P. R. Zimmerman, J. F. Boatman, J. D. Ray, and D. H. Stedman, 1987: Thunderstorms: An important mechanism in the transport of air pollutants. *Science*, **235**, 460–465.

Edwards, J. M. and A. Slingo, 1996: Studies with a flexible new radiation code. I: Choosing a configuration for a large-scale model. *Quart. J. Roy. Met. Soc.*, **122**, 689–719.

Ek, M. B., K. E. Mitchell, Y. Lin, E. Rogers, P. Grunmann, V. Koren, G. Gayno, and J. D. Tarpley, 2003: Implementation of Noah land surface model advances in the National Centers for Environmental Prediction operational mesoscale Eta model. *J. Geophys. Res.*, **108**, D22/8851.

Essery, R. L. H., M. J. Best, R. A. Betts, C. P. M., and C. M. Taylor, 2003: Explicit representation of subgrid heterogeneity in a GCM land-surface scheme. *J. Hydromet.*, **4**, 530–543.

Etling, D. and R. A. Brown, 1993: Roll vortices in the planetary boundary layer: A review. *Boundary-Layer Meteorol.*, **65**, 215–248.

Farr, T. G., P. A. Rosen, E. Caro, R. Crippen, R. Duren, S. Hensley, M. Kobrick, M. Paller, E. Rodriguez, L. Roth, D. Seal, S. Shaffer, J. Shimada, J. Umland, M. Werner, M. Oskin,

D. Burbank, and D. Alsdorf, 2007: The Shuttle Radar Topography Mission. *Rev. Geophys.*, **45**, RG2004.

Folkins, I., 2002: Origin of lapse rate changes in the upper tropical troposphere. *J. Atm. Sci.*, **59**, 992–1005.

Folkins, I., K. K. Kelly, and E. M. Weinstock, 2002: A simple explanation for the increase in the relative humidity between 11 and 14 km in the tropics. *J. Geophys. Res.*, **107**, D23/4736.

Folkins, I., M. Loewenstein, J. Podolske, S. J. Oltmans, and M. Proffitt, 1999: A barrier to vertical mixing at 14 km in the tropics: Evidence from ozonesondes and aircraft measurements. *J. Geophys. Res.*, **104**, 22095–22102.

Forster, P. and K. P. Shine, 1999: Stratospheric water vapour changes as a possible contributor to observed stratospheric cooling. *Geophys. Res. Lett.*, **26**, 3309–3312.

Fovell, R. G. and P. S. Dailey, 2001: Numerical simulation of the interaction between the sea-breeze front and horizontal convective rolls. Part II: Alongshore ambient flow. *Mon. Weath. Rev.*, **129**, 2057–2072.

Friedl, M. A., D. K. McIver, J. C. F. Hodges, X. Y. Zhang, D. Muchoney, A. H. Strahler, C. E. Woodcock, S. Gopal, A. Schneider, A. Cooper, A. Baccini, F. Gao, and C. Schaaf, 2002: Global land cover mapping from MODIS: algorithms and early results. *Remote Sens. Environ.*, **83**, 287–302.

Fueglistaler, S. and P. H. Haynes, 2005: Control of interannual and longer-term variability of stratospheric water vapor. *J. Geophys. Res.*, **110**, D24108.

Gettelman, A. and T. Birner, 2007: Insights into tropical tropopause layer processes using global models. *J. Geophys. Res.*, **112**, D23104.

Gettelman, A., J. Harries, and P. W. Mote, 2000: Distribution and variability of water vapour in

the upper troposphere and lower stratosphere. *SPARC assessment of upper tropospheric and stratospheric water vapour*, D. Kley, J. M. Russell III, and C. Phillips, eds., World Meteorological Organization, Geneva, Switzerland, volume WMO/TD No. 1043, SPARC Report No. 2 of *WCRP-113*, chapter 3, 196–264.

Gettelman, A. and A. H. Sobel, 2000: Direct diagnoses of stratosphere-troposphere exchange. *J. Atm. Sci.*, **57**, 3–16.

Golding, B. W., 1992: An efficient non-hydrostatic forecast model. *Met. Atm. Phys.*, **50**, 89–103.

— 1993: A numerical investigation of tropical island thunderstorms. *Mon. Weath. Rev.*, **121**, 1417–1433.

Gray, W. M. and R. W. Jacobson, Jr., 1977: Diurnal variation of deep cumulus convection. *Mon. Weath. Rev.*, **105**, 1171–1188.

Gregory, D. and P. R. Rowntree, 1990: A mass flux convection scheme with representation of cloud ensemble characteristics and stability-dependent closure. *Mon. Weath. Rev.*, **118**, 1483–1506.

Grell, G. A. and D. Dévényi, 2002: A generalized approach to parameterizing convection combining ensemble and data assimilation techniques. *Geophys. Res. Lett.*, **121**, D14/1693.

Grosvenor, D. P., T. W. Choularton, H. Coe, and G. Held, 2007: A study of the effect of overshooting deep convection on the water content of the TTL and lower stratosphere from Cloud Resolving Model simulations. *Atmos. Chem. Phys.*, **7**, 4977–5002.

Hamilton, K., R. A. Vincent, and P. T. May, 2004: Darwin Area Wave Experiment (DAWEX) field campaign to study gravity wave generation and propagation. *J. Geophys. Res.*, **109**, D20S01.

Hastings, D. A. and P. K. Dunbar, 1998: Development and assessment of the Global Land One-km Base Elevation digital elevation model (GLOBE). *ISPRS Archives*, **32**, 218–221.

Highwood, E. J. and B. J. Hoskins, 1998: The tropical tropopause. *Quart. J. Roy. Met. Soc.*, **124**, 1574–1604.

Holland, G. J., J. L. McBride, R. K. Smith, D. Jasper, and T. D. Keenan, 1986: The BMRC Australian Monsoon Experiment: AMEX. *Bull. Am. Met. Soc.*, **67**, 1466–1472.

Holton, J. R. and A. Gettelman, 2001: Horizontal transport and the dehydration of the stratosphere. *Geophys. Res. Lett.*, **28**, 2799–2802.

Holton, J. R., P. H. Haynes, M. E. McIntyre, A. R. Douglass, R. B. Rood, and L. Pfister, 1995: Stratosphere-troposphere exchange. *Rev. Geophys.*, **33**, 403–440.

Hong, S.-Y., Y. Noh, and J. Dudhia, 2006: A new vertical diffusion package with an explicit treatment of entrainment processes. *Mon. Weath. Rev.*, **134**, 2318–2341.

Houze, Jr., R. A., S. G. Geotis, F. D. Marks, Jr., and A. K. West, 1981: Winter monsoon convection in the vicinity of North Borneo. Part I: Structure and time variation of clouds and precipitation. *Mon. Weath. Rev.*, **109**, 1595–1614.

Jensen, E. J., A. S. Ackerman, and J. A. Smith, 2007: Can overshooting convection dehydrate the tropical tropopause layer? *J. Geophys. Res.*, **112**, D11209.

Jensen, E. J., L. Pfister, A. S. Ackerman, and A. Tabazadeh, 2001: A conceptual model of the dehydration of air due to freeze-drying by optically thin, laminar cirrus rising slowly across the tropical tropopause. *J. Geophys. Res.*, **106**, 17237–17252.

Keenan, T. D. and L. R. Brody, 1988: Synoptic-scale modulation of convection during the Australian summer monsoon. *Mon. Weath. Rev.*, **116**, 71–85.

Keenan, T. D. and R. E. Carbone, 1992: A preliminary morphology of precipitation systems in tropical northern Australia. *Quart. J. Roy. Met. Soc.*, **118**, 283–326.

Keenan, T. D., B. Ferrier, and J. Simpson, 1994: Development and structure of a Maritime Conti-

nent thunderstorm. *Met. Atm. Phys.*, **53**, 185–222.

Keenan, T. D., K. Glasson, F. Cummings, T. S. Bird, J. Keeler, and J. Lutz, 1998: The BMRC/NCAR C-band polarimetric (C-POL) radar system. *J. Atmos. Oceanic Technol.*, **15**, 871–886.

Keenan, T. D., J. McBride, G. Holland, N. Davidson, and B. Gunn, 1989a: Diurnal variations during the Australian Monsoon Experiment (AMEX) Phase II. *Mon. Weath. Rev.*, **117**, 2535–2552.

Keenan, T. D., B. R. Morton, M. J. Manton, and G. J. Holland, 1989b: The Island Thunderstorm Experiment (ITEX) – A study of tropical thunderstorms in the Maritime Continent. *Bull. Am. Met. Soc.*, **70**, 152–159.

Keenan, T. D., B. R. Morton, X. S. Zhang, and K. Nyguen, 1990: Some characteristics of thunderstorms over Bathurst and Melville Islands near Darwin, Australia. *Quart. J. Roy. Met. Soc.*, **116**, 1153–1172.

Keenan, T. D., S. Rutledge, R. Carbone, J. Wilson, T. Takahashi, P. May, N. Tapper, M. Platt, J. Hacker, S. Sekelsky, M. Moncrieff, K. Saito, G. Holland, A. Crook, and K. Gage, 2000: The Maritime Continent Thunderstorm Experiment (MCTEX): Overview and some results. *Bull. Am. Met. Soc.*, **81**, 2433–2455.

Keith, D. W., 2000: Stratosphere-troposphere exchange: Inferences from the isotopic composition of water vapor. *J. Geophys. Res.*, **105**, 15167–15173.

Kelly, K. K., M. H. Proffitt, K. R. Chan, M. Loewenstein, J. R. Podolske, S. E. Strahan, J. C. Wilson, and D. Kley, 1993: Water vapor and cloud water measurements over Darwin during the STEP 1987 tropical mission. *J. Geophys. Res.*, **98**, 8713–8723.

Kingsmill, D. E., 1995: Convection initiation associated with a sea-breeze front, a gust front and

their interaction. *Mon. Weath. Rev.*, **123**, 2913–2933.

Kirk-Davidoff, D. B., E. J. Hintsa, J. G. Anderson, and D. W. Keith, 1999: The effect of climate change on ozone depletion through changes in stratospheric water vapour. *Nature*, **402**, 399–401.

Kley, D., A. L. Schmeltekopf, K. Kelly, R. H. Winkler, T. L. Thompson, and M. McFarland, 1982: Transport of water through the tropical tropopause. *Geophys. Res. Lett.*, **9**, 617–620.

Kraus, E. B., 1963: The diurnal precipitation change over the sea. *J. Atm. Sci.*, **20**, 551–556.

Kritz, M. A., S. W. Rosner, K. K. Kelly, M. Loewenstein, and R. Chan, 1993: Radon measurements in the lower tropical stratosphere: Evidence for rapid vertical transport and dehydration of tropospheric air. *J. Geophys. Res.*, **98**, 8725–8736.

Kuang, Z. and C. S. Bretherton, 2004: Convective influence on the heat balance of the tropical tropopause layer: a cloud-resolving model study. *J. Atm. Sci.*, **61**, 2919–2927.

Kuettner, J. P., 1971: Cloud bands in the earth's atmosphere: Observations and theory. *Tellus*, **23**, 404–426.

Kullgren, K. and K.-Y. Kim, 2006: Physical mechanisms of the Australian summer monsoon: 1. Seasonal cycle. *J. Geophys. Res.*, **111**, D20104.

Küpper, C., J. Thuburn, G. C. Craig, and T. Birner, 2004: Mass and water transport into the tropical stratosphere: A cloud-resolving simulation. *J. Geophys. Res.*, **109**, D10111.

Liu, C. and M. W. Moncrieff, 1996: A numerical study of the effects of ambient flow and shear on density currents. *Mon. Weath. Rev.*, **124**, 2282–2303.

Liu, C. and E. J. Zipser, 2005: Global distribution of convection penetrating the tropical tropopause. *J. Geophys. Res.*, **110**, D23104.

Lock, A. P., A. R. Brown, M. R. Bush, G. M. Martin, and R. N. B. Smith, 2000: A new

boundary layer mixing scheme. Part I: Scheme description and single column model tests. *Mon. Weath. Rev.*, **128**, 3177–3199.

Loveland, T. R., B. C. Reed, J. F. Brown, D. O. Ohlen, J. Zhu, L. Yang, and J. W. Merchant, 2000: Development of a global land cover characteristics database and IGBP DISCover from 1-km AVHRR data. *Int. J. Remote Sensing*, **21**, 1303–1330.

Marécal, V., E. D. Rivière, G. Held, S. Cautenet, and S. Freitas, 2006: Modelling study of the impact of deep convection on the utls air composition – Part I: Analysis of ozone precursors. *Atmos. Chem. Phys.*, **6**, 1567–1584.

May, P. T. and A. Ballinger, 2007: The statistical characteristics of convective cells in a monsoon regime (Darwin, Northern Australia). *Mon. Weath. Rev.*, **135**, 82–92.

May, P. T., J. H. Mather, G. Vaughan, C. Jakob, G. M. McFarquhar, K. N. Bower, and G. G. Mace, 2008: The Tropical Warm Pool International Cloud Experiment. *Bull. Am. Met. Soc.*, **89**, 629–645.

May, P. T. and D. K. Rajopadhyaya, 1999: Vertical velocity characteristics of deep convection over Darwin, Australia. *Mon. Weath. Rev.*, **127**, 1056–1071.

McBride, J. L., 1987: The Australian summer monsoon. *Monsoon Meteorology*, C. P. Chang and T. N. Krishnamurti, eds., Clarendon Press, Oxford, UK, 60–92.

Mote, P. W., K. H. Rosenlof, M. E. McIntyre, E. S. Carr, J. C. Gille, J. R. Holton, J. S. Kinnersley, H. C. Pumphrey, J. M. Russell III, and J. W. Waters, 1996: An atmospheric tape recorder: The imprint of tropical tropopause temperatures on stratospheric water vapor. *J. Geophys. Res.*, **101**, 3989–4006.

Newell, R. E. and S. Gould-Stewart, 1981: A stratospheric fountain? *J. Atm. Sci.*, **38**, 2789–2796.

Oliphant, A. J., A. P. Sturman, and N. J. Tapper, 2001: The evolution and structure of a tropical

island sea/land breeze system, northern Australia. *Met. Atm. Phys.*, **78**, 45–59.

Pommereau, J.-P., A. Garnier, G. Held, and 39 co-authors, 2007: An overview of the HIBISCUS campaign. *Atmos. Chem. Phys. Discuss.*, **7**, 2389–2475.

Potter, B. E. and J. R. Holton, 1995: The role of monsoon convection in the dehydration of the lower tropical stratosphere. *J. Atm. Sci.*, **52**, 1034–1050.

Ramage, C. S., 1968: Role of a tropical "Maritime Continent" in the atmospheric circulation. *Mon. Weath. Rev.*, **96**, 365–370.

Read, W. G., D. L. Wu, J. W. Waters, and H. C. Pumphrey, 2004: Dehydration in the tropical tropopause layer: Implications from the UARS Microwave Limb Sounder. *J. Geophys. Res.*, **109**, D06110.

Reid, G. C. and K. S. Gage, 1996: The tropical tropopause over the western Pacific: Wave driving, convection, and the annual cycle. *J. Geophys. Res.*, **101**, 21233–21241.

Riehl, H. and J. S. Malkus, 1958: On the heat balance in the equatorial trough zone. *Geophysica*, **6**, 503–538.

Rivière, E. D., V. Marécal, N. Larsen, and S. Cautenet, 2006: Modelling study of the impact of deep convection on the UTLS air composition – Part 2: Ozone budget in the TTL. *Atmos. Chem. Phys.*, **6**, 1585–1598.

Robinson, F. J. and S. C. Sherwood, 2006: Modeling the impact of convective entrainment of the tropical tropopause. *J. Atm. Sci.*, **63**, 1013–1027.

Robinson, F. J., S. C. Sherwood, and Y. Li, 2008: Resonant response of deep convection to surface hot spots. *J. Atm. Sci.*, **65**, 276–286.

Russell, P. B., L. Pfister, and H. B. Selkirk, 1993: The tropical experiment of the Stratosphere-Troposphere Exchange Project (STEP): Science objectives, operations, and summary findings.

J. Geophys. Res., **98**, 8563–8589.

Saito, K. and T. Kato, 1999: The Meteorological Research Institute mesoscale nonhydrostatic model (in japanese). Meteorology Research Note 196, Meteorological Society of Japan, Tokyo, Japan, 169-195.

Saito, K., T. Keenan, G. Holland, and K. Puri, 2001: Numerical simulation of the diurnal evolution of tropical island convection over the Maritime Continent. *Mon. Weath. Rev.*, **129**, 378–400.

Schafer, R., P. T. May, T. D. Keenan, K. McGuffie, W. L. Ecklund, P. E. Johnston, and K. S. Gage, 2001: Boundary layer development over a tropical island during the Maritime Continent Thunderstorm Experiment. *J. Atm. Sci.*, **58**, 2163–2179.

Schumann, U., 2005: TROCCINOX – Tropical Convection, Cirrrus and Nitrogen Oxides Experiment, Overview. *Proc. of the 2nd General Assembly of the European Geosciences Union*, Apr. 24–29, 2005, Vienna, Austria, *Geophys. Res. Abs.*, **7**, 11180.

Sherwood, S. C. and A. E. Dessler, 2000: On the control of stratospheric humidity. *Geophys. Res. Lett.*, **27**, 2513–2516.

— 2001: A model for transport across the tropical tropopause. *J. Atm. Sci.*, **58**, 765–779.

Sherwood, S. C., T. Horinouchi, and H. A. Zeleznik, 2003: Convective impact of temperatures observed near the tropical tropopause. *J. Atm. Sci.*, **60**, 1847–1856.

Simpson, J., T. D. Keenan, B. Ferrier, R. H. Simpson, and G. J. Holland, 1993: Cumulus mergers in the maritime continent region. *Met. Atm. Phys.*, **51**, 73–99.

Skamarock, W. C., J. B. Klemp, J. Dudhia, D. O. Gill, D. M. Barker, W. Wang, and J. G. Powers, 2007: A description of the Advanced Research WRF Version 2. NCAR Technical Note NCAR/TN-468+STR, NCAR, Boulder, CO, USA, 100 pp.

Skinner, T. and N. Tapper, 1994: Preliminary sea breeze studies over Bathurst and Melville

Islands, northern Australia, as part of the island thunderstorm experiment (ITEX). *Met. Atm. Phys.*, **53**, 77–94.

Stauffer, D. R. and N. Seaman, 1990: Use of Four-Dimensional Data Assimilation in a limited-area mesoscale model. Part I: Experiments with synoptic-scale data. *Mon. Weath. Rev.*, **118**, 1250–1277.

Steiner, M., R. A. Houze, and S. E. Yuter, 1995: Climatological characterization of three dimensional storm structure from operational radar and rainguage data. *J. Appl. Meteor.*, **34**, 1978–2007.

Teitelbaum, H., M. Moustaoui, C. Basdevant, and J. R. Holton, 2000: An alternative mechanism explaining the hygropause formation in tropical regions. *Geophys. Res. Lett.*, **27**, 221–224.

Thompson, G., P. R. Field, W. D. Hall, and R. M. Rasmussen, 2006: A new bulk microphysical parameterization for WRF (& MM5). *Proc. of the 8th WRF Users' Workshop*, Jun. 11–15, 2007, Boulder, CO, USA.

Thompson, G., R. M. Rasmussen, and K. Manning, 2004: Explicit forecasts of winter precipitation using an improved bulk micro-physics scheme. Part I: Description and sensitivity analysis. *Mon. Weath. Rev.*, **132**, 519–542.

Thuburn, J. and G. C. Craig, 2002: On the temperature structure of the tropical substratosphere. *J. Geophys. Res.*, **107**, D2/4017.

Tsuda, T., M. V. Ratnam, P. T. May, M. J. Alexander, R. A. Vincent, and A. MacKinnon, 2004: Characteristics of gravity waves with short vertical wavelengths observed with radiosonde and GPS occultation during DAWEX (Darwin Area Wave Experiment). *J. Geophys. Res.*, **109**, D20S03.

Vaughan, G., C. Schiller, A. R. MacKenzie, K. Bower, T. Peter, H. Schlager, N. R. P. Harris,

and P. T. May, 2008: SCOUT-O3/ACTIVE: High-altitude aircraft measurements around deep tropical convection. *Bull. Am. Met. Soc.*, **89**, 647–662.

Vömel, H., S. J. Oltmans, D. Kley, and P. J. Crutzen, 1995: New evidence for the stratospheric dehydration mechanism in the equatorial pacific. *Geophys. Res. Lett.*, **22**, 3235–3238.

Webster, P. J. and R. A. Houze Jr., 1991: The Equatorial Mesoscale Experiment (EMEX): An overview. *Bull. Am. Met. Soc.*, **72**, 1481–1505.

Whiteway, J., C. Cook, M. Gallagher, T. Choularton, J. Harries, P. Connolly, R. Busen, K. Bower, M. Flynn, P. May, R. Aspey, and J. Hacker, 2004: Anatomy of cirrus clouds: Results from the Emerald airborne campaigns. *Geophys. Res. Lett.*, **31**, L24102.

Wilson, D. R. and S. P. Ballard, 1999: A microphysically based precipitation scheme for the UK Meteorological Office Unified Model. *Quart. J. Roy. Met. Soc.*, **125**, 1607–1636.

Wilson, J. W., R. E. Carbone, J. D. Tuttle, and T. D. Keenan, 2001: Tropical island convection in the absence of significant topography. Part II: Nowcasting storm evolution. *Mon. Weath. Rev.*, **129**, 1637–1655.

Wilson, J. W., G. B. Foote, N. A. Crook, J. C. Frankhauser, C. G. Wade, J. D. Tuttle, C. K. Mueller, and S. K. Krueger, 1992: The role of boundary-layer convergence zones and horizontal rolls in the initiation of thunderstorms: A case study. *Mon. Weath. Rev.*, **120**, 1785–1815.

Zhou, X. L., A. Geller, and M. H. Zhang, 2001: Tropical cold point tropopause characteristics derived from ECMWF reanalyses and soundings. *J. Climate*, **14**, 1823–1838.

Zöger, M., A. Afchine, N. Eicke, M.-T. Gerhards, E. Klein, D. S. McKenna, U. Mörschel, U. Schmidt, V. Tan, F. Tuitjer, T. Woyke, and C. Schiller, 1999: Fast in situ stratospheric hygrometers: A new family of balloon-borne and airborne Lyman α photofragment fluorescence hygrometers. *J. Geophys. Res.*, **104**, 1807–1816.

Figure Captions

FIG. 1. Orography of the Tiwi Islands. The attached color scale indicates altitude in meters above mean sea level (a.m.s.l.). The dashed polylines represent the areas of the domains ARW3, UM3, and ARW4 (see text and Table 1).

FIG. 2. Standard US Air Force Skew-T Log-p diagram plotted from the sounding taken in Darwin, Australia, on November 30, 2005 at 1430 LT (Local Time).

FIG. 3. Brightness temperature (BT) at 10.8 μm from MTSAT-1R satellite imagery over the area of Darwin, Australia, on November 30, 2005 at 1000 LT (*a*), 1600 LT (*b*), and 2200 LT (*c*). Typically, high clouds are characterized by the lowest BT at 10.8 μm. Streamlines at 850 hPa derived from ECMWF analyses are superimposed.

FIG. 4. Vertical velocity field w at 125 above ground level (a.g.l.) simulated by ARW (left-hand column) and UM (right-hand column) in domains ARW3 and UM3, respectively, at 1400 LT ((*a*) and (*b*)), 1500 LT ((*c*) and (*d*)), 1600 LT ((*e*) and (*f*)), and 1700 LT ((*g*) and (*h*)). Horizontal wind vectors at 10 m a.g.l. are superimposed. The black line (A–B) on the plots (*e*) and (*f*) gives the position of the vertical cross section in Figures 7 and 8(*c*).

FIG. 5. Sensible heat flux simulated by ARW (left-hand column) and UM (right-hand column) in domains ARW3 and UM3, respectively, at 1400 LT ((*a*) and (*b*)), 1500 LT ((*c*) and (*d*)), 1600 LT ((*e*) and (*f*)), and 1700 LT ((*g*) and (*h*)). Horizontal wind vectors at 10 m above ground level are

superimposed.

FIG. 6. Hourly-averaged precipitation rate derived from the BMRC/NCAR C-POL radar measurements (first row) and simulated by ARW (second row) and UM (third row) in domains ARW3 and UM3, respectively, at 1500 LT ((*a*), (*c*) and (*e*)) and 1600 LT ((*b*), (*d*) and (*f*)). The flight track of the M55-Geophysica research aircraft on November 30, 2005, from 1500 LT to 1700 LT is superimposed on the plots (*a*) and (*b*) and is discussed in § 5.b. Horizontal wind vectors at 10 m above ground level are superimposed on the plots (*c*) to (*f*).

FIG. 7. Vertical cross section along the line A–B in Figures 4(*e*) and 4(*f*): (*a*) microphysical classification from the BMRC/NCAR C-POL radar measurements at 1430 LT; (*b*) rain (orange), cloud liquid water (black), graupel (purple), and ice (green) mixing ratios simulated by ARW at 1600 LT in the domain ARW3, with 0.5, 0.5, 1, and 0.1-g kg^{-1} interval contours, respectively; (*c*) same caption as (*b*) for UM in the domain UM3, except with 1-g kg^{-1} interval contours for the cloud liquid water and total ice mixing ratios. The attached color scale for plots (*b*) and (*c*) indicates vertical velocity in m s^{-1}.

FIG. 8. Same caption as Figure 4(*e*), Figure 6(*d*), and Figure 7(*b*) for ARW in the domain ARW4.

FIG. 9. Scattergrams θ–H_2O using observational data from the FISH hygrometer on board of the M55-Geophysica research aircraft on November 19 (blue and black) and 30 (orange and red), 2005 (see text for flight times and Figures 6(*a*) and 6(*b*) for the flight track on November 30, 2005, from 1500 LT to 1700 LT). Black and red colors are used to emphasize points for which total water

RH_{ice} is greater than 150 %, indicating clearly the presence of ice particles.

FIG. 10. Scattergrams θ–H_2O using results from the ARW (left-hand column) and UM (right-hand column) simulations in domains ARW3 and UM3, respectively, at 1230 LT ((*a*) and (*b*)), 1530 LT ((*c*) and (*d*)), 1830 LT ((*e*) and (*f*)), and 2130 LT ((*g*) and (*h*)). The red color is used to emphasize points for which total water RH_{ice} is greater than 150 %, indicating clearly the presence of ice particles.

FIG. 11. Moistening computed using results from ARW and UM over the domains ARW3 and UM3, respectively, as the difference between the mean water vapor mixing ratios within 5-K virtual potential temperature bins at 1830 LT (a couple of hours after Hector had formed) and at 1530 LT (during the mature stage of Hector). The blue shaded bars correspond to the ARW simulation starting on November 28, 2005 at 0930 LT, while the stipple-filled bars correspond to the one starting on November 29, 2005 at 0930 LT. The red hachured bars correspond to the UM simulation. Note that the two models have their own separate 'y axis'.

Figures

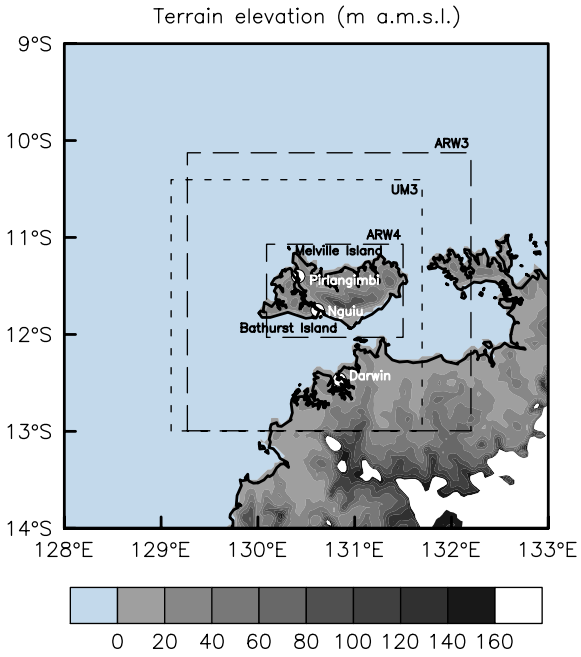

FIG. 1. Orography of the Tiwi Islands. The attached color scale indicates altitude in meters above mean sea level (a.m.s.l.). The dashed polylines represent the areas of the domains ARW3, UM3, and ARW4 (see text and Table 1).

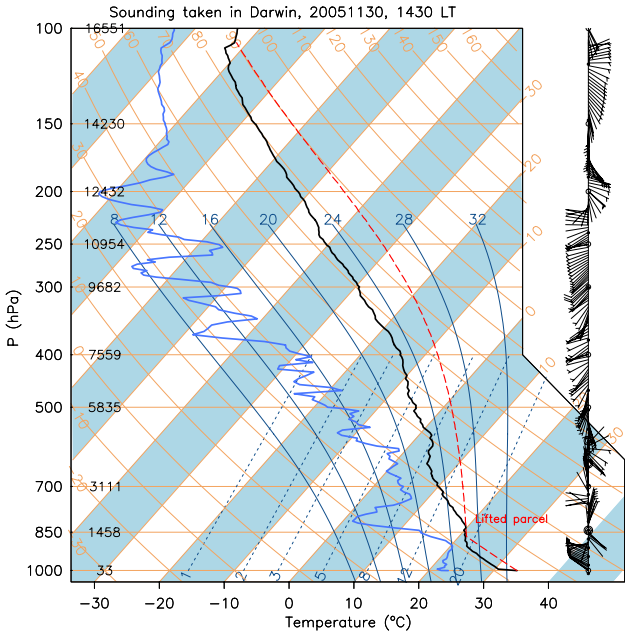

FIG. 2. Standard US Air Force Skew-T Log-p diagram plotted from the sounding taken in Darwin, Australia, on November 30, 2005 at 1430 LT (Local Time).

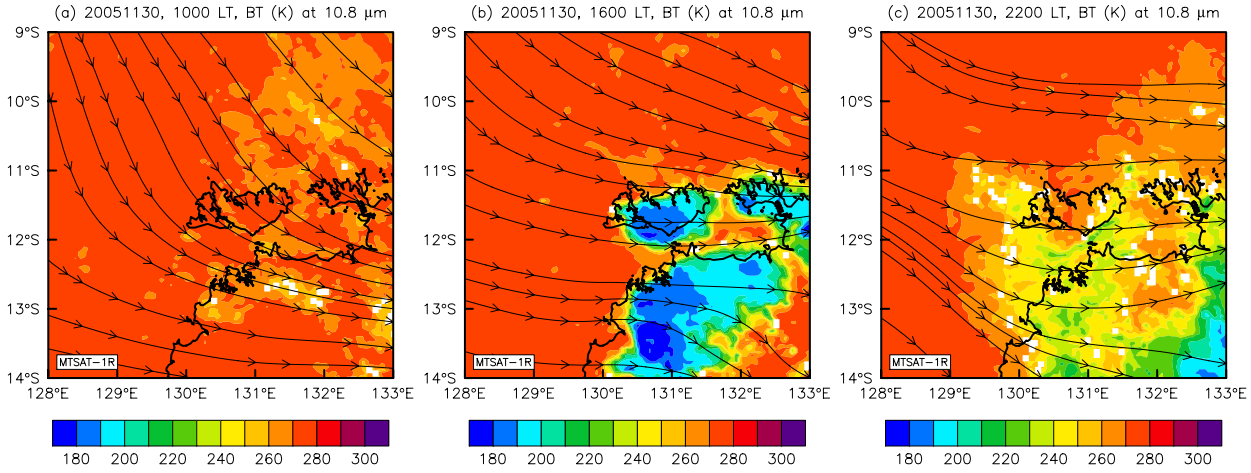

FIG. 3. Brightness temperature (BT) at 10.8 μm from MTSAT-1R satellite imagery over the area of Darwin, Australia, on November 30, 2005 at 1000 LT (*a*), 1600 LT (*b*), and 2200 LT (*c*). Typically, high clouds are characterized by the lowest BT at 10.8 μm. Streamlines at 850 hPa derived from ECMWF analyses are superimposed.

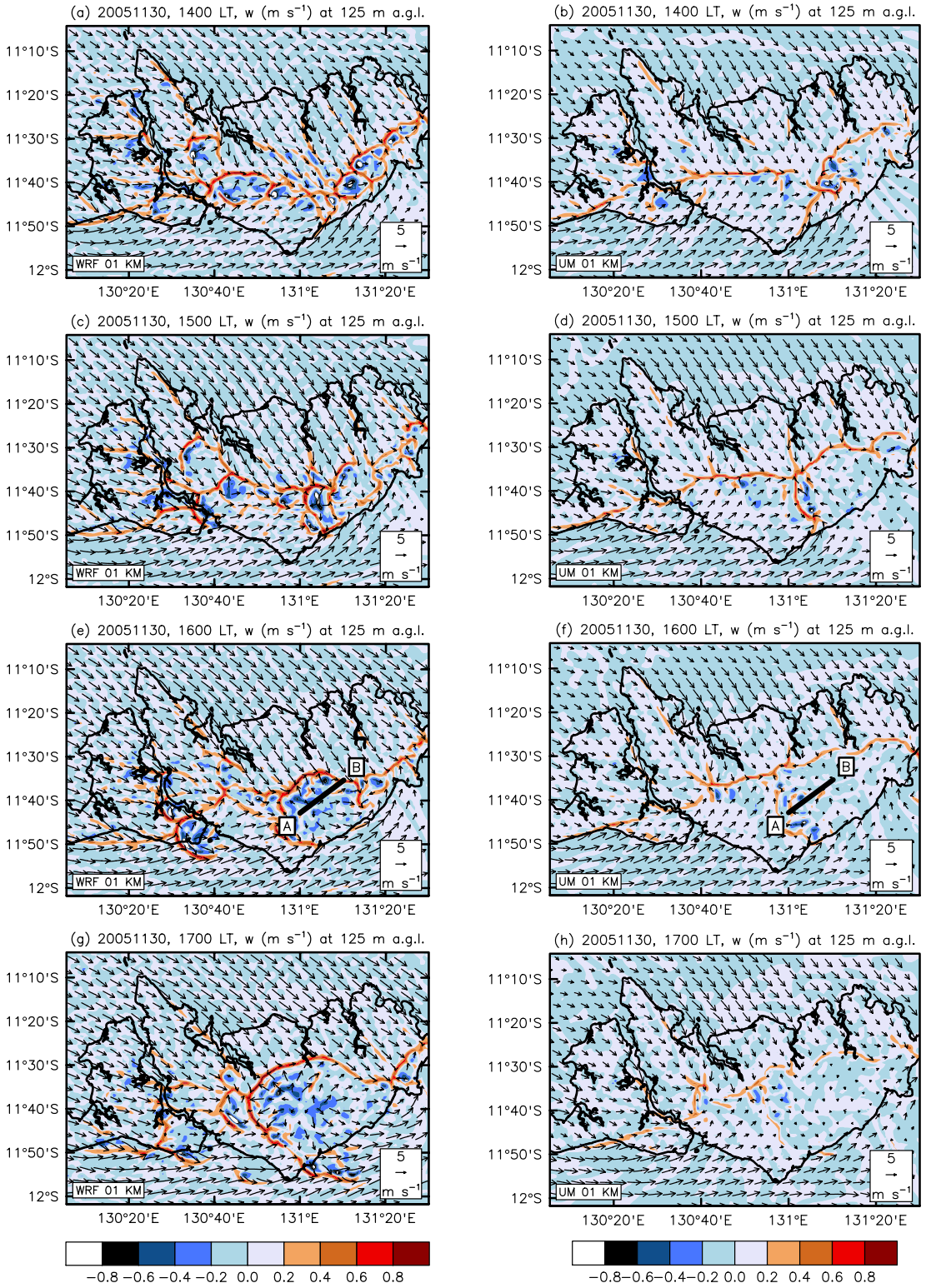

FIG. 4. Vertical velocity field w at 125 above ground level (a.g.l.) simulated by ARW (left-hand column) and UM (right-hand column) in domains ARW3 and UM3, respectively, at 1400 LT ((*a*) and (*b*)), 1500 LT ((*c*) and (*d*)), 1600 LT ((*e*) and (*f*)), and 1700 LT ((*g*) and (*h*)). Horizontal wind vectors at 10 m a.g.l. are superimposed. The black line (A–B) on the plots (*e*) and (*f*) gives the position of the vertical cross section in Figures 7 and 8(*c*).

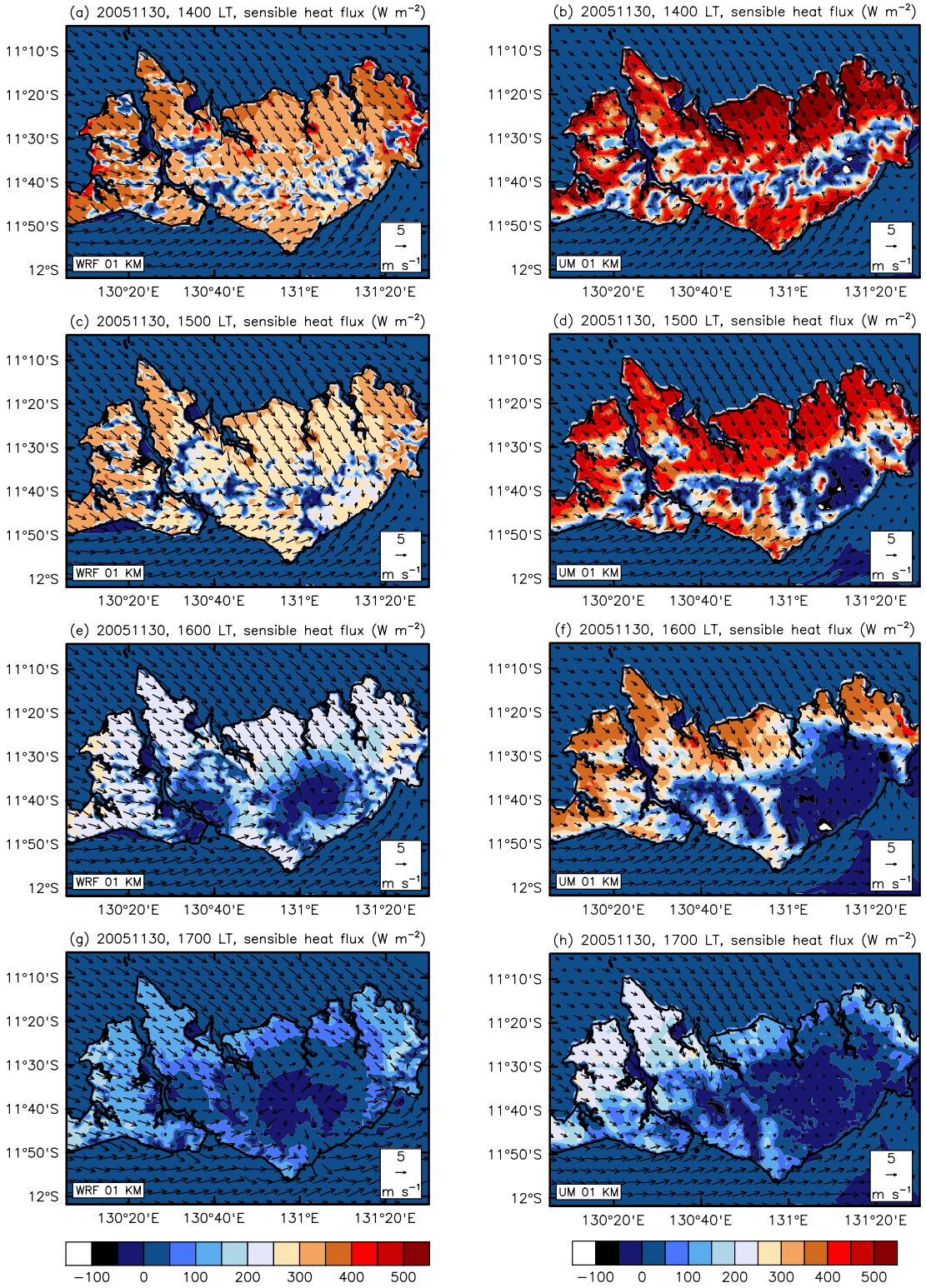

FIG. 5. Sensible heat flux simulated by ARW (left-hand column) and UM (right-hand column) in domains ARW3 and UM3, respectively, at 1400 LT ((*a*) and (*b*)), 1500 LT ((*c*) and (*d*)), 1600 LT ((*e*) and (*f*)), and 1700 LT ((*g*) and (*h*)). Horizontal wind vectors at 10 m above ground level are superimposed.

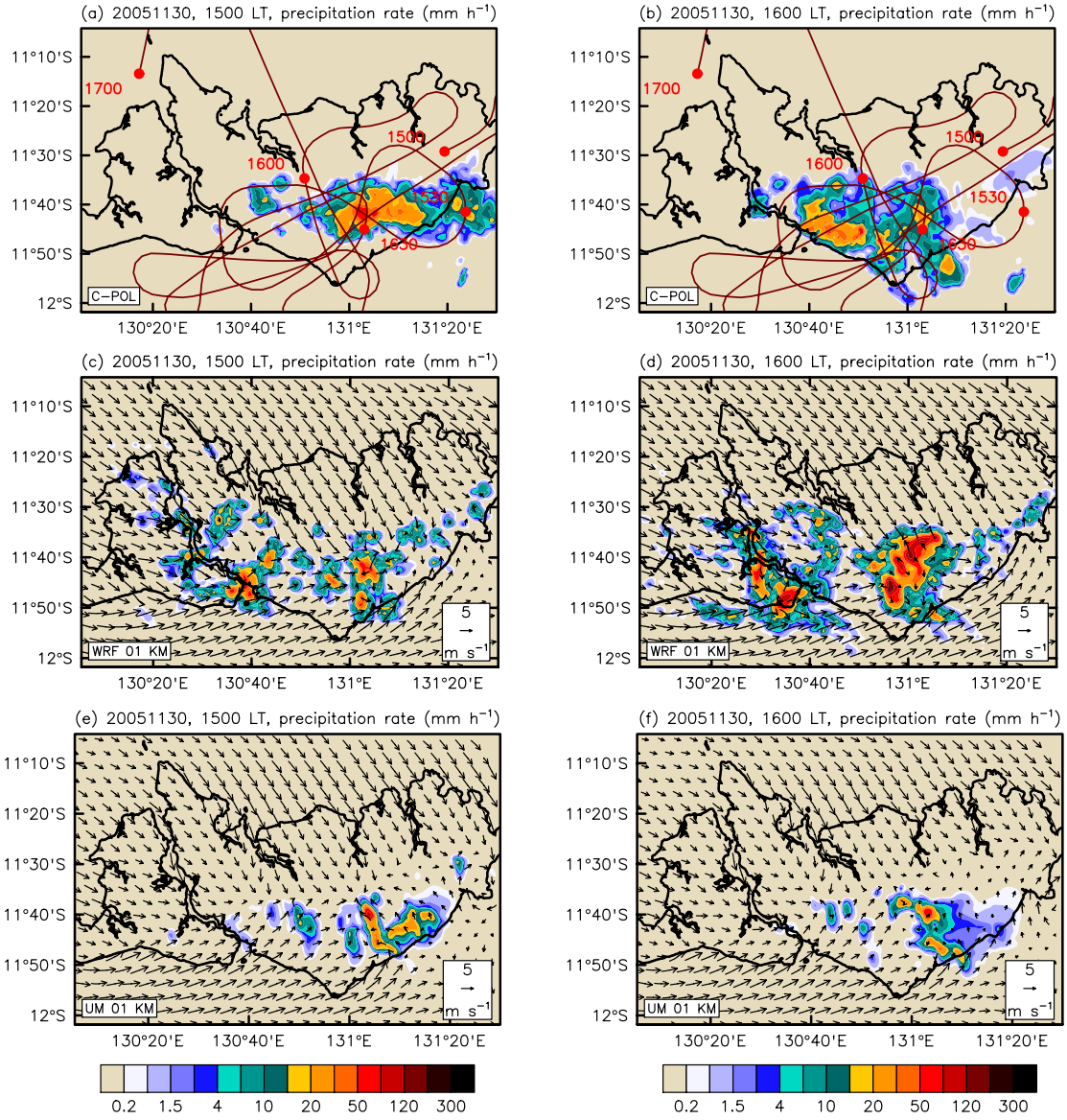

FIG. 6. Hourly-averaged precipitation rate derived from the BMRC/NCAR C-POL radar measurements (first row) and simulated by ARW (second row) and UM (third row) in domains ARW3 and UM3, respectively, at 1500 LT ((*a*), (*c*) and (*e*)) and 1600 LT ((*b*), (*d*) and (*f*)). The flight track of the M55-Geophysica research aircraft on November 30, 2005, from 1500 LT to 1700 LT is superimposed on the plots (*a*) and (*b*) and is discussed in § 5.b. Horizontal wind vectors at 10 m above ground level are superimposed on the plots (*c*) to (*f*).

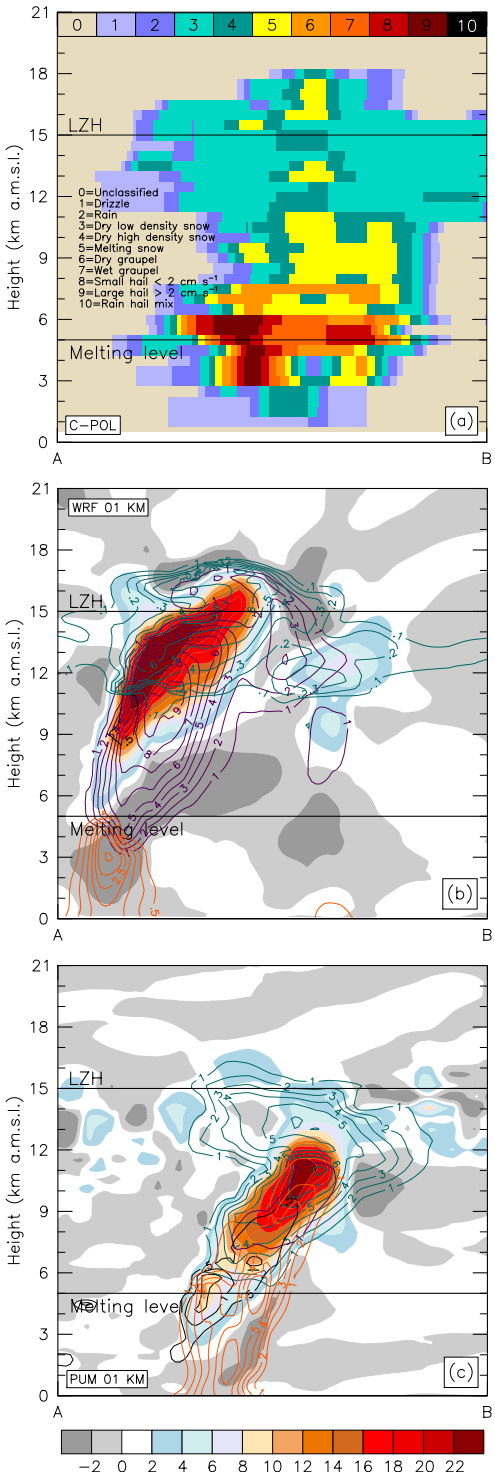

FIG. 7. Vertical cross section along the line A–B in Figures 4(*e*) and 4(*f*): (*a*) microphysical classification from the BMRC/NCAR C-POL radar measurements at 1430 LT; (*b*) rain (orange), cloud liquid water (black), graupel (purple), and ice (green) mixing ratios simulated by ARW at 1600 LT in the domain ARW3, with 0.5, 0.5, 1, and 0.1-g kg^{-1} interval contours, respectively; (*c*) same caption as (*b*) for UM in the domain UM3, except with 1-g kg^{-1} interval contours for the cloud liquid water and total ice mixing ratios. The attached color scale for plots (*b*) and (*c*) indicates vertical velocity in m s^{-1}.

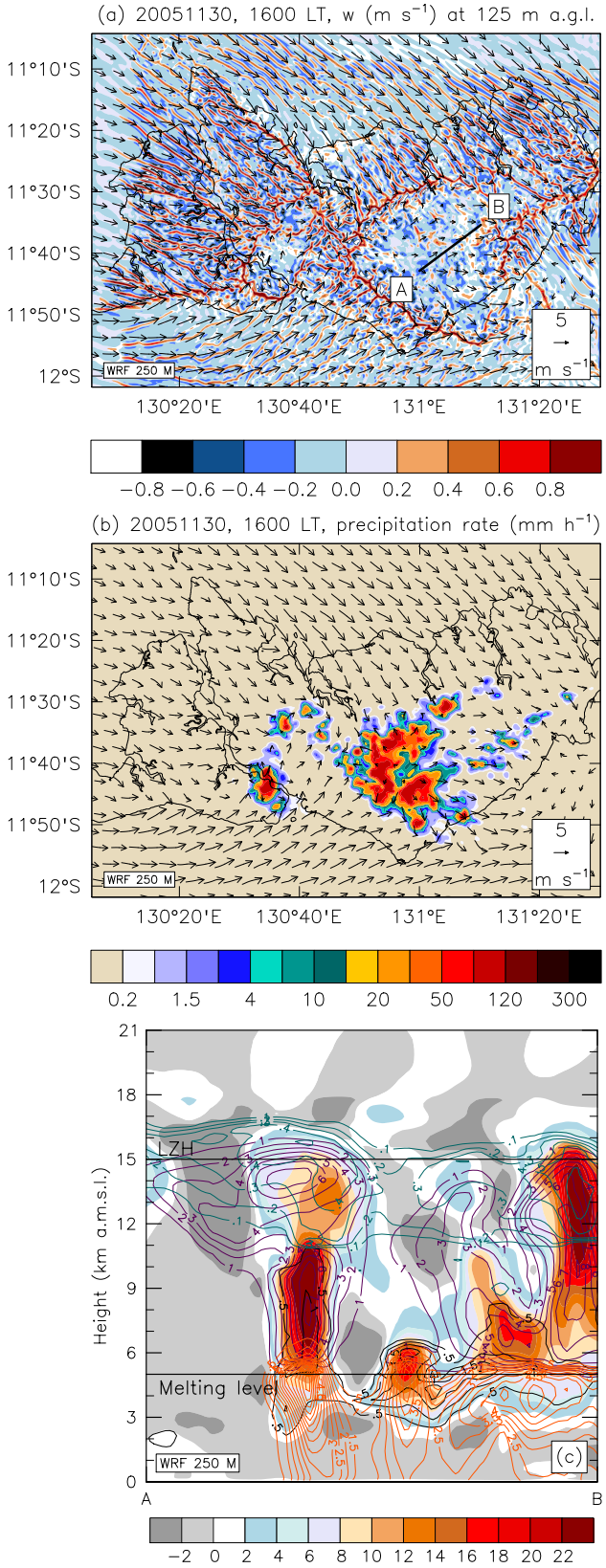

FIG. 8. Same caption as Figure 4(*e*), Figure 6(*d*), and Figure 7(*b*) for ARW in the domain ARW4.

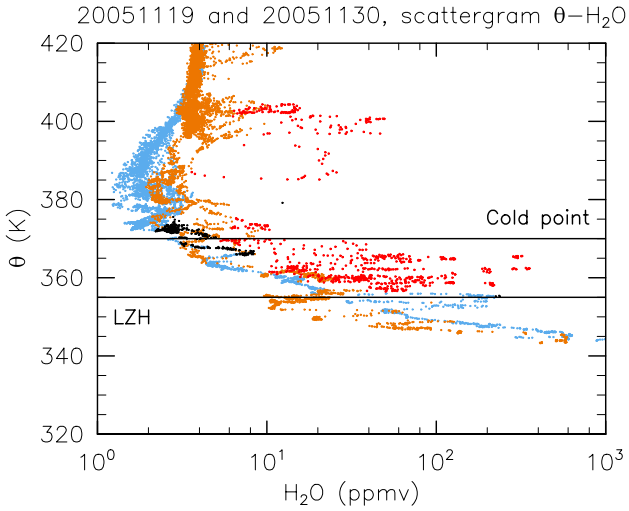

FIG. 9. Scattergrams θ–H_2O using observational data from the FISH hygrometer on board of the M55-Geophysica research aircraft on November 19 (blue and black) and 30 (orange and red), 2005 (see text for flight times and Figures 6(*a*) and 6(*b*) for the flight track on November 30, 2005, from 1500 LT to 1700 LT). Black and red colors are used to emphasize points for which total water RH_{ice} is greater than 150 %, indicating clearly the presence of ice particles.

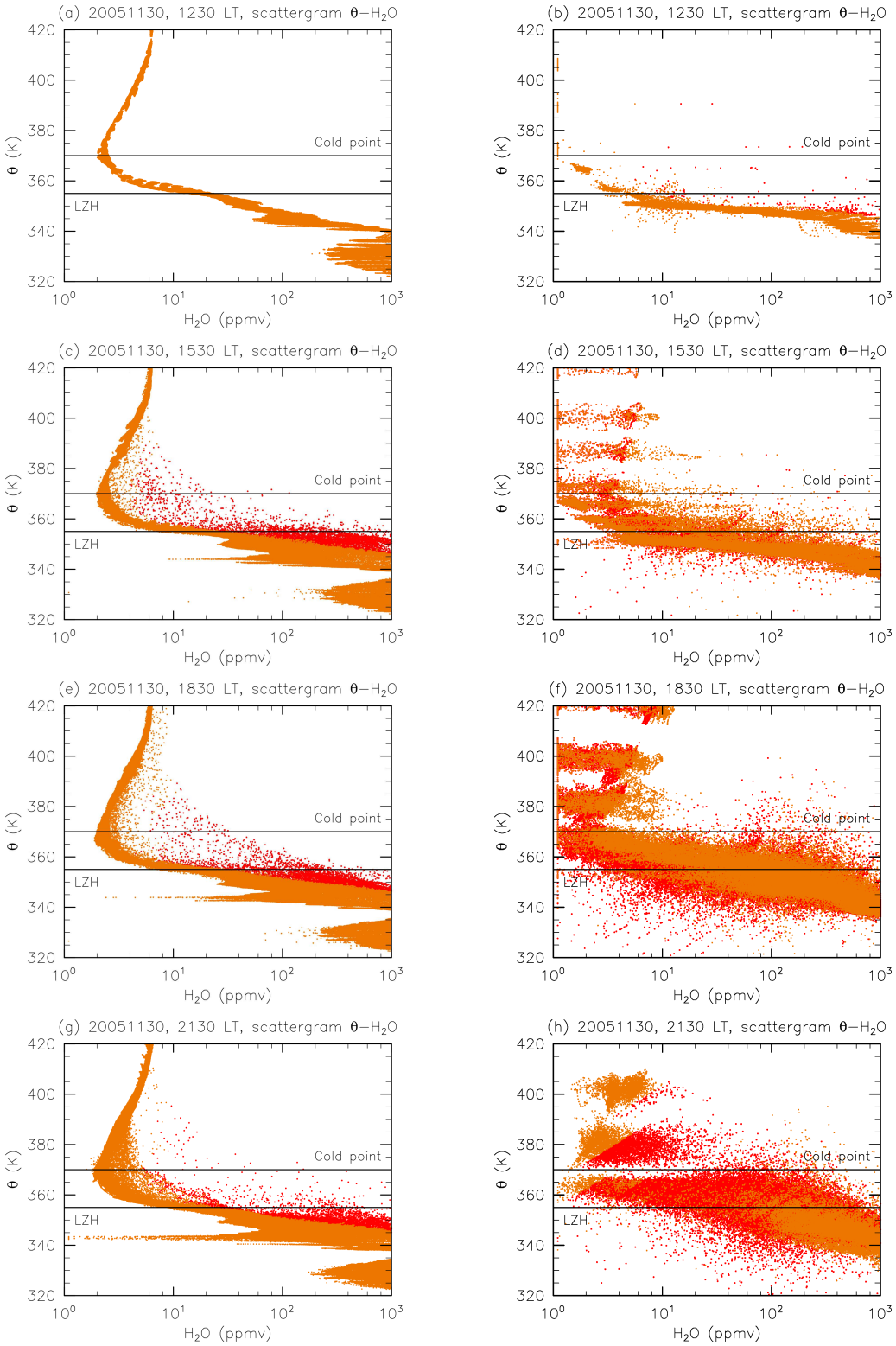

FIG. 10. Scattergrams θ–H_2O using results from the ARW (left-hand column) and UM (right-hand column) simulations in domains ARW3 and UM3, respectively, at 1230 LT ((*a*) and (*b*)), 1530 LT ((*c*) and (*d*)), 1830 LT ((*e*) and (*f*)), and 2130 LT ((*g*) and (*h*)). The red color is used to emphasize points for which total water RH_{ice} is greater than 150 %, indicating clearly the presence of ice particles.

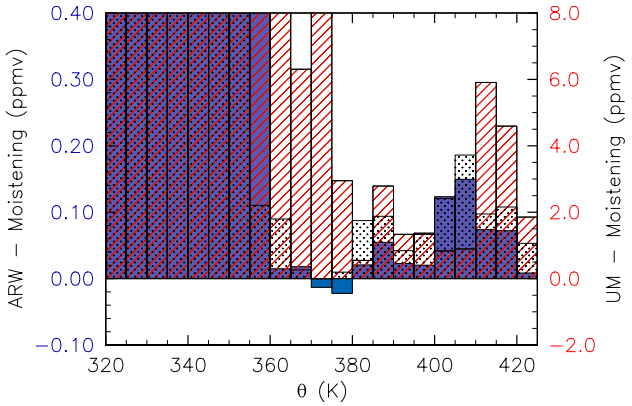

FIG. 11. Moistening computed using results from ARW and UM over the domains ARW3 and UM3, respectively, as the difference between the mean water vapor mixing ratios within 5-K virtual potential temperature bins at 1830 LT (a couple of hours after Hector had formed) and at 1530 LT (during the mature stage of Hector). The blue shaded bars correspond to the ARW simulation starting on November 28, 2005 at 0930 LT, while the stipple-filled bars correspond to the one starting on November 29, 2005 at 0930 LT. The red hachured bars correspond to the UM simulation. Note that the two models have their own separate 'y axis'.

Tables

Table 1. Resolution of the grids used for the simulations.

Domain	Typical extent	Grid points (E-W, N-S)	Grid size
UM0	Globe	432, 324	$5/6$, $5/9°$
ARW1	Northern Territory	141, 141	16 km
UM1		320, 320	$0.11°$
ARW2	Area of Darwin	221, 221	4 km
UM2		310, 200	$0.036°$
ARW3	Tiwi Islands (Large)	341, 341	1 km
UM3		290, 290	$0.009°$
ARW4	Tiwi Islands (Small)	621, 621	250 m